FLORIDA STATE UNIVERSITY

COLLEGE OF ARTS AND SCIENCES

UNDERSTANDING MAGNETIC EXCHANGE BEHAVIOR IN CORE@SHELL NANOPARTICLES

By

DAVID J CARNEVALE JR

A Dissertation submitted to the
Department of Chemistry and Biochemistry
in partial fulfillment of the
requirements for the degree of
Doctor of Philosophy

2017

David Carnevale defended this dissertation on November 20, 2017.
The members of the supervisory committee were:

Michael Shatruk
Professor Co-Directing Dissertation

Geoffrey F. Strouse
Professor Co-Directing Dissertation

Peng Xiong
University Representative

Joseph Schlenoff
Committee Member

The Graduate School has verified and approved the above-named committee members, and certifies that the dissertation has been approved in accordance with university requirements.

Dedicated to Kate and Lily, this work is only possible thanks to your continued love and support.

ACKNOWLEDGMENTS

This work was done with the help of both the Shatruk and Strouse groups. Whether it be fielding my constant questions or simply just providing pleasant conversation, each and every person in both groups have contributed in some way. In particular, I want to thank Jeff Lengyel. Jeff has been a constant help with not only with his intellect, but also with his time in helping with different data collections and processing.

Thanks to the joint wisdom of both Dr. Shatruk and Dr. Strouse, I have been able to work on a difficult project that I can take pride in. Through their understanding and insight of the project, we have been able to make significant strides in understanding magnetic exchange behavior. While it was not always easy for the three of us to agree on the science, the work was made all the better once we settled on the answers.

I also thank my wife, Kate, for her endless support and patience while I wrote and prepared this dissertation. Whether through the times I was stressed and panicked, or simply was locked in my office working until all hours of the night, Kate was understanding and thoughtful.

Finally, I'd like to thank my family and friends back home for their support and love. Even when times have been tough in grad school, they've always provided a safe haven for me to take refuge.

TABLE OF CONTENTS

List of Tables vii
List of Figures viii
Abstract xi

1. INTRODUCTION 1
    1.1 Magnetic Nanoparticles 1
    1.2 Nanomagnetism 8
    1.3 Magnetic Exchange Coupling 11
    1.4 Generating Core@Shell Nanomaterials 14
    1.5 Microwave Reactors 16
    1.6 Research Objectives 17

2. MATERIALS AND METHODS 19
    2.1 Starting Materials 19
    2.2 Synthesis 19
    2.3 Physical Measurements 22

3. EVOLUTION OF EXCHANGE COUPLING BEHAVIOR IN 5 NM FEPT PARTICLES WITH VARIABLE COBALT SHELL THICKNESSESS 25
    3.1 Introduction 25
    3.2 Results and Discussion 28
    3.3 Conclusion 43

4. EVOLUTION OF EXCHANGE COUPLING BEHAVIOR IN CORE@SHELL MATERIALS WITH VARIABLE CORE SIZES 45
    4.1 Introduction 45
    4.2 Results and Discussion 46
    4.3 Conclusion 56

5. STUDYING ALTERNATIVE SHELLING ELEMENTS ON A 5 NM FEPT NANOPARTICLE 58
    5.1 Introduction 58
    5.2 Results and Discussion 59
    5.3 Conclusion 65

6. THE SYNTHESIS OF OTHER HARD MAGNETIC NANOPARTICLES 66
    6.1 Introduction 66
    6.2 Results and Discussion 67
    6.3 Conclusion 71

7. CONCLUSION AND OUTLOOK 73

References..76

Biographical Sketch 82

LIST OF TABLES

Table 3.1 The metal content in of the FePt and FePt@Co nanoparticles as determined from the ICP-MS analysis. 29

Table 4.1 XRF data for comparable shell sizes in each series of particles. 51

Table 5.1 Estimated shortest and longest thicknesses of the FePt@Ni system based on the total particle size 64

Table 7.1 Unit cell parameters and Curie temperature of Fe_3Se_4 and Cr_3Te_4...............................75

LIST OF FIGURES

Figure 1.1 The attractive effect of a paramagnetic material on an applied magnetic field (a) and the repulsive effect that occurs when a field is applied to a diamagnet (b). 2

Figure 1.2 Magnetically ordered states: ferromagnetic (a), antiferromagnetic (b), and ferrimagnetic ordering (c). 3

Figure 1.3 Temperature dependence of magnetic susceptibility (left) and inverse magnetic susceptibility (right) for a paramagnetic material (dashed), a ferromagnetic material (green), and an antiferromagnetic material (red). 4

Figure 1.4 Isothermal field dependence of magnetization for a hard magnet (a) and a soft magnet (b). 5

Figure 1.5 The general process of domain growth to incorporate more moments as a stronger external field is applied until all moments in the material are aligned along the field. 8

Figure 1.6 The change in coercivity as a function of particle size..9

Figure 1.7 Left: the difference between the ZFC (blue) and FC (red) temperature-dependent magnetization of a nanomaterial. Right: the field-dependent magnetization of a material below (dashed line) and above (solid line) the blocking temperature. 9

Figure 1.8 The energy product (BH) of a hard magnet (dashed) can be increased by controllably mixing it with a soft magnet and generating an exchange-spring magnet (solid). 11

Figure 1.9 Differences in the demagnetization/remagnetization behavior between a conventional hard magnet (a) and an exchange-spring magnet (b). 12

Figure 1.10 The role of cooling field in the behavior of an exchange bias material. 13

Figure 3.1 HR-TEM images of the $Fe_{0.65}Pt_{0.35}$ cores (a, d) and the core-shell nanoparticles with the 1.2 nm (b, e) and the 2.7 nm (c, f) Co shell. 28

Figure 3.2 Size histograms measured for FePt/Co core-shell nanoparticles with the (a) 0 nm, (b) 0.6 nm, (c) 1.0 nm, (d) 1.2 nm, (e) 1.7 nm, (f) 2.0 nm, and (g) 2.7 nm thick Co shells. 30

Figure 3.3 IR spectrum of 4.9 nm FePt. 31

Figure 3.4 Dielectric spectroscopy of oleylamine/oleic acid mixtures. 31

Figure 3.5 TGA curves measured on the $Fe_{0.65}Pt_{0.35}$ cores (a) and the $Fe_{0.65}Pt_{0.35}$@Co nanoparticles with a 1nm thick Co shell. 32

Figure 3.6 From left to right: pictograms, HR-TEM images, pXRD patterns, isothermal (5 K) hysteresis loops, and isofield (10 mT) ZFC-FC magnetization curves of the fcc-FePt/Co core/shell nanoparticles, in the order of increasing Co shell thickness: (a) 0 nm, (b) 0.6 nm, (c) 1.0 nm, (d) 1.2 nm, (e) 1.7 nm, (f) 2.0 nm and, (g) 2.7 nm. 33

Figure 3.7 Dielectric spectroscopy comparing the microwave permittivity of the solvent and the 5 nm FePt particles...35

Figure 3.8 Powder X-ray diffraction patterns of reaction products after attempts to obtain FePt/Co core-shell nanoparticles in a round bottom vessel at 300°C (a) and 150°C (b)..............36

Figure 3.9 The dependence of magnetic properties of FePt@Co nanoparticles on Co shell thickness: (a) saturation magnetization, M_s, (b) coercive field, H_c, (c) % remnant magnetization recovery, (e) energy product, BH, and (e) anisotropy constant, K_{eff}. 37

Figure 3.10 Magnetization recovery curves of the FePt nanoparticles (a) and the FePt/Co core-shell nanoparticles with 1.0 nm (b) and 2.7 nm (c) Co shell. 38

Figure 3.11 Field-dependent magnetization of FePt nanoparticles and FePt@Co nanoparticles with 1 nm Co shell immediately after the synthesis and after 3-year storage in open air. 41

Figure 3.12 Temperature dependences of ZFC/FC magnetization of the original (a) and 3 year old FePt sample (b). 42

Figure 3.13 Field-dependent magnetization of a FePt@Co sample initially worked up under N_2 atmosphere and then measured again after being held in ambient conditions for 2 weeks...........42

Figure 3.14 (a) A diagram of proposed magnetic exchange regimes that occur within the core-shell nanoparticles. (b) Hysteresis loops for FePt@Co nanoparticles with different Co shell thicknesses. 43

Figure 4.1 Powder XRD patterns of the 3.4 (top), 4.9 (middle), and 7.3 nm (bottom) FePt nanoparticles. 47

Figure 4.2 TEM of 3.4 nm (a), 4.9 nm (b), 7.3 nm (c), and 10 nm (d) FePt nanoparticles. 48

Figure 4.3 TEMs of the various core@shell particles. The top row shows an increasing shell size on the 3.4 nm cores. The middle and bottom rows correspond to the 4.9 and 7.3 nm cores, respectively. 49

Figure 4.4 Hysteresis loops of the 3.4, 4.9, and 7.3 nm FePt cores, along with their 1 and 2 nm shells. 52

Figure 4.5 The evolution of Ms with increasing shell size. The saturation moment data is fit to a power law consistent with an expected r^3 volume scaling...53

Figure 4.6 The change in Hc with increasing shell size (a) as well as the combined coercivity data after normalizing to the parent core (b). A simple polynomial fit is used as a guide to the eye for (a). The normalized data has been fit to a sine curve in order to determine how well it compares to the idea of a helical spin 53

Figure 4.7 Hysteresis loops of the 3.4@2 nm shell, 4.9@1nm shell, and 7.3 nm cores..............54

Figure 4.8 The energy product of the different particles, normalized to the 5 nm FePt@1 nm Co shell. The 3.4 nm cores are represented in red, the 4.9 nm cores are blue, and the 7.3 nm cores are green. 55

Figure 5.1 ZFC and FC of the 0.9 nm shelled FePt@Ni particles. 60

Figure 5.2 STEM images of the 1.5 nm shell (a), and two different angles of the 2 nm shells (b&c), as well as pictorials of the core to shell orientations (d-f), where (e) has a general depiction of the difference in direction between the Ni moments (blue) and FePt moments (red) based on their respective anisotropies...61

Figure 5.3 Summary of blocking temperature (a), saturation moment (b), and coercivity (c) due to increasing shell thickness of the nickel. The fit of the saturation moment follows an r^3 power law. 62

Figure 5.4 Corner-edge and edge-corner distances can be calculated using Pythagorean theorem. The corner-edge distance can be found given the total particle size is known and the core size is known, however the edge-corner distance can only be solved after c for triangle A is found......63

Figure 6.1 Structure of endo-[$Fe(CO)_3SePh]_2$. 68

Figure 6.2 XRD pattern for the 10 nm $SmCo_5$ nanoparticles. The Sm_2O_3 and hcp-Co impurities are marked, while the hkl planes are given for the $SmCo_5$...69

Figure 6.3 XRD pattern of the mixed Fe_3Se_4/Fe_7Se_8 sample. The underlined and bolded hkl labels correspond to the Fe_7Se_8 and Fe_3Se_4 reflections, respectively 69

Figure 6.4 TEM of the 10 ± 2 nm $SmCo_5$ particles (left) and the 22 ± 3 nm Fe_3Se_4 particles (right) 70

Figure 6.5 ZFC (solid) and FC (dashed) curves for the $SmCo_5$ (left) and the 250 K field sweep (right). The $SmCo_5$ particles show a blocking temp of 6 K and a coercivity of 0.35 T... 71

Figure 6.6 ZFC (solid) and FC (dashed) curves for Fe_xSe_y (left) and the 250 K field sweep (right). 71

ABSTRACT

As green technology advances, the need for cheaper, stronger permanent magnets becomes more and more vital. Electric motors, like those used in wind turbines and electric cars, rely heavily on Dy-doped $Nd_2Fe_{14}B$ in order to achieve the required energy conversion efficiencies, but both Nd and Dy are expensive rare-earth elements that pose the risk of supply chain disruption. To mitigate this issue, research efforts have focused on combining powerful lanthanide-containing permanent magnets with cheaper and more abundant soft magnetic materials. This combination should afford so-called exchange-spring magnets, which will be less expensive and more energy-efficient. While exchange coupling behavior between hard and soft magnetic materials has been studied for several decades, little is known about such exchange on the scale of nanoparticles. There also exist significant problems with controlling the size and composition uniformity in the generated materials, leading to the limited understanding of the properties of these assemblies.

In order to address both of these issues, we devised an approach to create a hard magnetic nanoparticle of fcc-FePt, which was then covered with the soft magnetic shell of Co. In order to gain the desired synthetic control over the final size and shape of core@shell particles, a combination of round bottom and microwave heating techniques was utilized, the synthetic details of which are laid out in Chapter 2. Chapter 3 describes the results of structural and magnetic characterization of the 5-nm FePt nanoparticles covered with the Co shell of varying thickness. In Chapter 4, the effect of changing the core size were studied. From this work, we were able to find confirmation of previous theories that the overall exchange effects are limited by the soft magnetic component. Regardless of the properties of the core material, we found that the exchange properties were limited in distance, with the maximum properties dropping off for the shell size of ~1nm and continually declining as the shell size increased to 2 nm. Most significant is the finding

that the coercivity is enhanced to a maximum of ~235% for all core-shell particles, as compared to the coercivity of unshelled FePt particles. This means the coupling is related to the intrinsic properties of the materials and not the physical volume or surface areas that we might expect at the nanoscale.

Chapter 5 reports the results of varying the chemical nature of the magnetic shell from cobalt to nickel, which leads to a substantial change in the observed magnetic properties. Due to the unfavorable “diagonal” growth of the shell onto the cores, the coercive enhancement cannot be properly ascertained, as the smallest shell produces a thickness that is greater than 2 nm at some angles, which is outside the expected limits of the exchange capabilities. The decreased saturation magnetization, however, gives some insight into the issues of differences in anisotropy of two materials composing the hybrid core-shell nanoparticles. The different magnetocrystalline anisotropies, along with the canted crystal growth produce an overall particle with weaker magnetism than the core along.

With the aim to extend these studies to other hard magnets, Chapter 6 describes the synthesis and characterization of 10 nm $SmCo_5$ and 22 nm Fe_3Se_4 nanoparticles. Fe_3Se_4 was prepared through both conventional and microwave heating methods, while $SmCo_5$ was only prepared using microwave synthesis. While the initial reactions of these materials seemed promising, reproducibility and particle size control still represent major challenges to overcome.

CHAPTER 1

INTRODUCTION

1.1 Magnetic Nanoparticles

1.1.1 Magnetic Ordering

Since the first discovery of lodestone, magnetic materials have been at the forefront of human interest in observed physical phenomena and their potential applications. Starting from a mechanically simple compass and progressing to the modern electric motor, humans have been relying on magnets for sensing, transportation, and energy conversion for centuries. However, while compasses were known of as early as 300-200 BC, magnetism was not truly studied until the early 1800s.[1] Owing to the work of some of the greatest scientists ever known, including Michael Faraday and James Maxwell, we now understand that magnetism is the result of the movement of electrons within a material and their response to an external electrical, magnetic, or electromagnetic field.[2,3] While the paired electrons are the source of diamagnetism, which repels the applied magnetic field, the sought after paramagnetic materials generate a positive/attractive response to the external field (Figure 1.1). The Meissner effect, which occurs in superconducting materials, is the case of perfect diamagnetism and results in a material that completely repels a magnetic field and gives rise to magnetic levitation.[4–6] While diamagnetism in intrinsic to all materials, it is paramagnetic materials that we are more commonly accustomed to thinking about when we talk about magnetism.

Paramagnetic materials that exhibit ordering of their unpaired electrons are classified as ferromagnets, antiferromagnets, and ferrimagnets (Figure 1.2). The temperature at which magnetic ordering occurs is referred to as the Curie temperature (T_C) in ferro- and ferrimagnets and the Neel temperature (T_N) in antiferromagnets. Ferromagnetism happens when it is energetically favorable for the electron spins to align parallel to one another, generating a net magnetic moment in the material even in the absence of applied magnetic field (spontaneous magnetization). Notable ferromagnets include the elemental metals, Fe, Co, Ni, and Gd, as well as the intermetallic compounds $SmCo_5$ and $Nd_2Fe_{14}B$.[7]

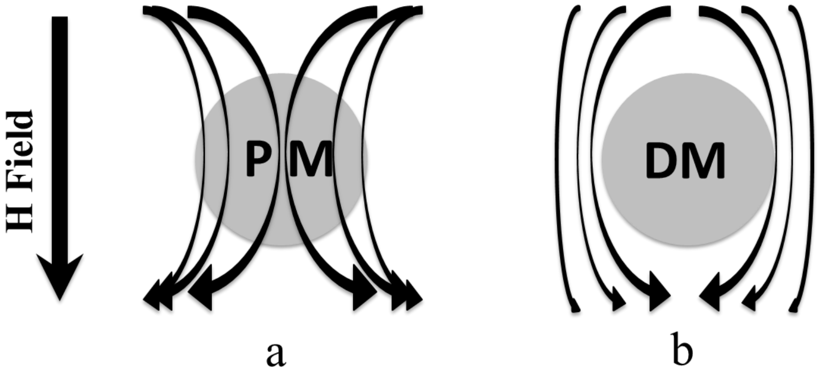

Figure 1.1 The attractive effect of a paramagnetic material (PM) on an applied magnetic field (a) and the repulsive effect that occurs when a field is applied to a diamagnet (DM) (b).

The antiferromagnetic state is achieved when the moments align antiparallel to one another, resulting in zero net magnetization. It is important to understand that while antiferromagnetic materials do not offer a net magnetic moment, they are distinctly different from diamagnetic materials, which repel (weaken) the applied field and result in a negative magnetization. Notable antiferromagnets include the simple oxides of ferromagnetic metals, FeO, CoO, and NiO. Ferrimagnetism is the antiparallel alignment of unequal spins, which result either from different valences of the same metal or from the mixing of two metals with different spin values in the same structure. As a result, the net magnetization of ferrimagnet is greater than zero but usually lower than in comparable ferromagnetic systems. The most common ferrimagnet used is Fe_3O_4, which contains antiparallelly arranged spins of two Fe^{3+} and one Fe^{2+} ions, making it impossible for the moments to fully cancel out.

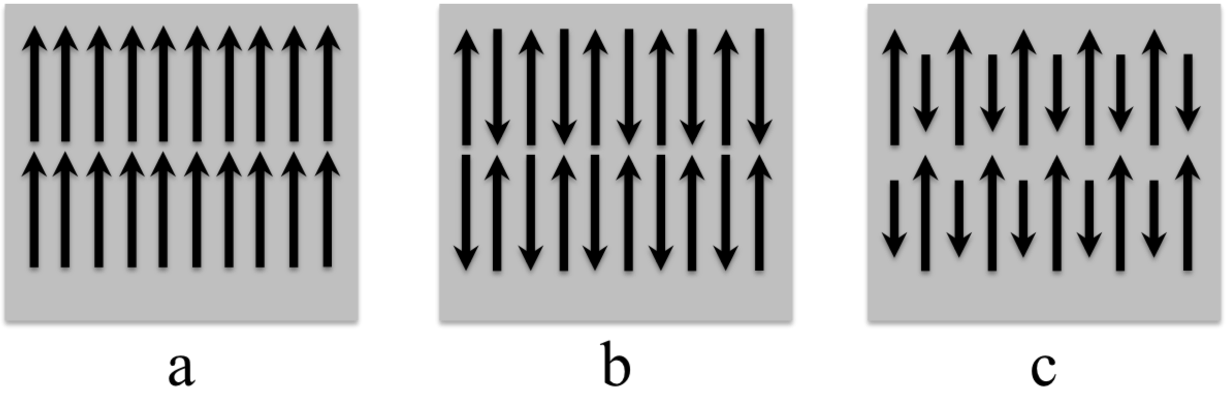

Figure 1.2 Magnetically ordered states: ferromagnetic (a), antiferromagnetic (b), and ferrimagnetic (c).

The overall magnetization (M) in a paramagnetic system depends on both temperature (T) and strength of the applied field (H). The ratio of M/H is called the magnetic susceptibility (χ) and, well above magnetic ordering temperature, can be described by the Curie law and the Curie constant (C):

$$c = \frac{C}{T} \tag{1}$$

$$C = \frac{Ng^2 {\mu_B}^2 S(S+1)}{3k_B} \text{ or } C = \frac{Ng^2 {\mu_B}^2 J(J+1)}{3k_B} \tag{2}$$

where N is Avogadro’s number, g is the Landé g-factor, μ_B is the Bohr magneton, S is the spin angular momentum, J is the total angular momentum, and k_B is the Boltzmann constant. The difference between the S and J terms in Eq 2 arises from the fact that transition metal ions are often described using only the S value of the system, while lanthanide ions exhibit much stronger coupling between the spin and orbital (L) angular momenta (spin-orbit coupling), necessitating the use of the total angular momentum (J) in the expression for the Curie law.

While the Curie law works well for some paramagnetic systems, a system that exhibit significant exchange coupling between magnetic centers will deviate from this equation. A correction introduced to account for the magnetic exchange is called the Weiss constant (θ) and gives rise to the Curie-Weiss law:

$$\chi = \frac{C}{T - \theta} \tag{3}$$

Paramagnetic materials with negligible magnetic interactions will have a θ = 0, while materials with ferromagnetic and antiferromagnetic nearest-neighbor exchange will have, respectively, positive and negative values of θ.

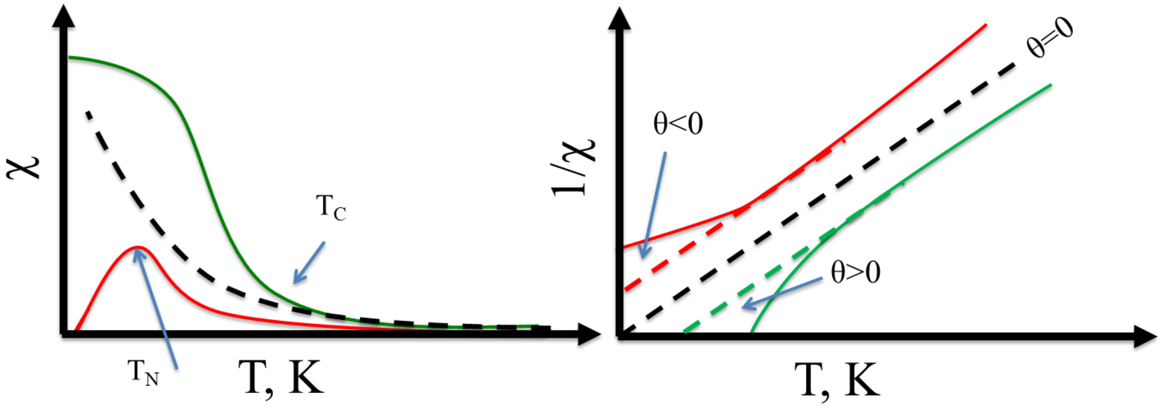

Figure 1.3 Temperature dependence of magnetic susceptibility (left) and inverse magnetic susceptibility (right) for a paramagnetic material (dashed), a ferromagnetic material (green), and an antiferromagnetic material (red).

Both the Weiss constant and ordering temperature of magnetic materials can be determined by measuring a temperature dependence of magnetization (magnetic susceptibility) at constant (usually low) magnetic field. The plots of the temperature dependence of magnetic susceptibility (χ vs T) and inverse magnetic susceptibility (1/χ vs T) allow determination of the ordering temperature and the Weiss constant, respectively (Figure 1.3).

1.1.2 Hard and Soft Magnetic Materials

While antiferromagnetic materials undergo an abrupt decrease in magnetization at the ordering temperature, ferromagnets and ferrimagnets behave drastically different. The key characteristics of a ferro- or ferrimagnetic material are saturation magnetization (M_s), remnant magnetization (M_r), coercivity (H_c), and energy product (BH). These parameters are found by performing isothermal field-dependent magnetization measurements. The comparison of these properties gives rise to the classification of magnets into hard and soft (Figure 1.4), where hard magnets are also referred to as "permanent magnets". Note that although we tend to refer to the magnetic polarization (M) as a measure of magnetic strength, we use the magnetic flux density (B) to compare energy product, as it gives a better representation of the magnetic field produced by a material.

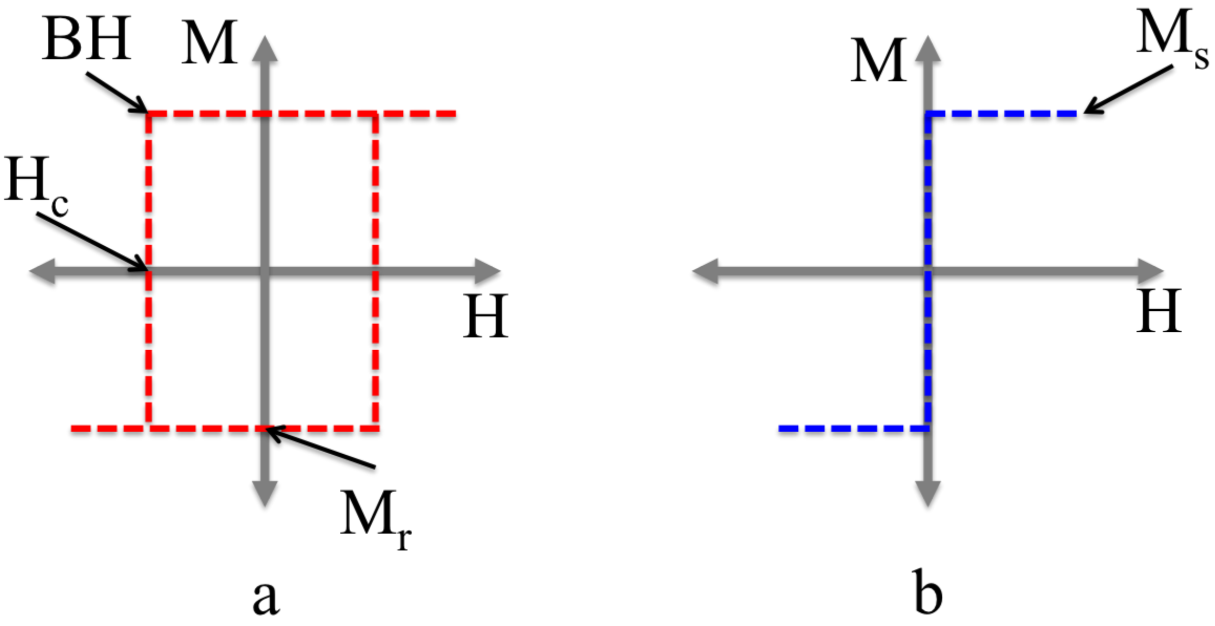

Figure 1.4 Isothermal field dependence of magnetization for a hard magnet (a) and a soft magnet (b).

Saturation magnetization is the highest magnetic value a material can achieve at a given temperature, occurring from a maximum alignment of the moments with the applied magnetic field. Because thermal fluctuations can prevent the system from complete magnetic ordering, it is important to characterize the material at sufficiently low temperature in order to achieve the full saturation of magnetization.

Remnant magnetization is simply the total magnetization left in a system when the applied field is turned off. While an ideal soft magnet should lose its magnetization completely when the field is turned off, in reality it is common for soft magnets to retain some albeit small magnetization value in zero field. Hard magnets, however, preserve substantial amount of their maximum magnetization value when the field is turned off.

While the values of M_r tend to differ drastically between hard and soft magnets, the true distinction between the two materials can be seen in the coercivity (H_c), defined as the point at which a sufficient demagnetizing magnetic field is applied to drive the magnetization of the system to zero. Hard magnets are described as such because the moments in the system are very "stiff", requiring a large field applied in the opposite direction in order to change the alignment of the moments. Typically magnets with $H_c \geq 0.1$ T are considered hard. Soft magnets have moments that easily switch their direction under action of an applied magnetic field. Such materials can be seen as soft or pliable because they can be demagnetized with magnetic fields lower than 0.01 T.

An important characteristic for the energy conversion is the energy product of the magnet, which is defined as the maximum product of magnetic flux by magnetic field (BH) along the demagnetization curve. The maximum energy product is used to determine the usefulness of permanent magnets in different applications, with high energy product materials being vital for current clean energy applications. The highest energy product materials known are $Nd_2Fe_{14}B$,

$SmCo_5$, and Sm_2Co_{17}, with room temperature energy products of ~50, 22, and 32 MGOe, respectively.[7] Commonly used soft magnetic materials are simple transition metals, Fe, Co, and Ni.

1.1.3 Magnetic Anisotropy

Magnetic anisotropy (K) is a measure of the amount of energy per unit area (J/m^3) that is required to realign the magnetic moments in a material and describes the energetic preference of magnetic moments to stay aligned in a certain direction. Because magnetic anisotropy is directly related to the coercivity of a material,

$$K = H_c M_s \tag{4}$$

hard magnetic materials have K values that are several orders of magnitude larger than those of soft magnetic materials, on the order of 10^6-10^7 and 10^4-10^5 J/m^3, respectively.[8] Heavier elements provide strong spin orbit coupling values that generates large magnetic anisotropy values. The coupling of the spin (S) and orbital angular (L) momenta is described by the spin-orbit coupling operator, with the spin-orbit coupling constant λ:

$$\hat{H}_{\mathrm{so}} = \lambda \hat{L} \hat{S} \tag{5}$$

The measure of preference for a moment to align along a particular crystalline axis is called the magnetocrystalline anisotropy. This anisotropy contribution often relies on the strongly anisotropic nature of local magnetic moments for particular metal ions. For examples, $SmCo_5$ and $Sm_2Fe_{17}N$ exhibit K values of 1.9×10^7 and 8.4×10^6 J/m^3, respectively, largely due to magnetocrystalline anisotropy of the Sm sites.[9] One reason for the high coercivity of $SmCo_5$ arises from the elongated c-axis of the hexagonal structure, which makes the coupling energy to the ab plane non-degenerate to the c-axis coupling. This difference in coupling energy makes it favorable for the moments to order along the c-axis, but more importantly, makes it extremely difficult to reverse the magnetization through the ab-plane .[9,10]

1.2 Nanomagnetism

1.2.1 Magnetic Domains

The demagnetization process in bulk magnets proceeds via the formation of domains and motion of domain walls. The structuring of a magnetically ordered materials in magnetic domains is due to the need to decrease magnetostatic energy that leads to unfavorable interaction of ordered magnetic moments with stray magnetic field generated by the material. At the critical temperature, the moments in each domain become ordered, but the orientation of the total moment of a domain differs from that of the neighboring domains (Figure 1.5). [11,12]

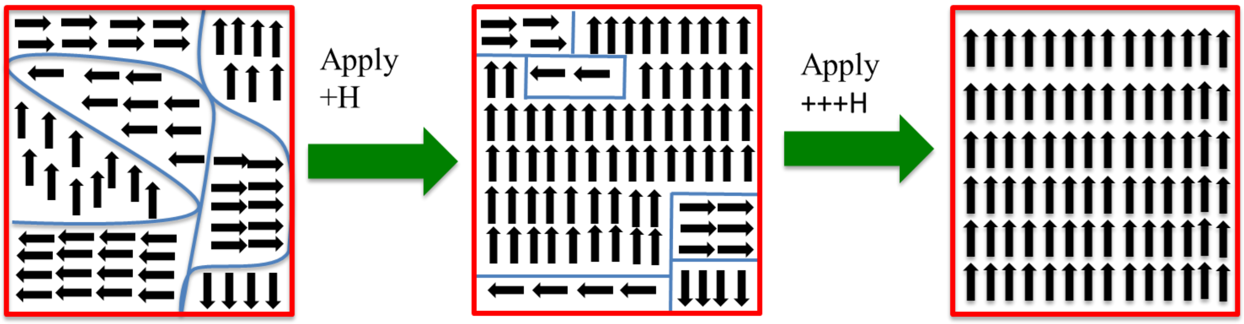

Figure 1.5 The general process of domain growth to incorporate more moments as a stronger external field is applied until all moments in the material are aligned along the field.

Typical domain sizes are on the order of nanometers. Therefore, a magnetic nanoparticle can be smaller than a domain size, giving rise to a particle that does not contain any domain walls. Particles at the single domain limit exhibit the highest coercivity (Figure 1.6) because the demagnetization can proceed only through the collective rotation of the strongly coupled magnetic moments rather than through domain wall movement.

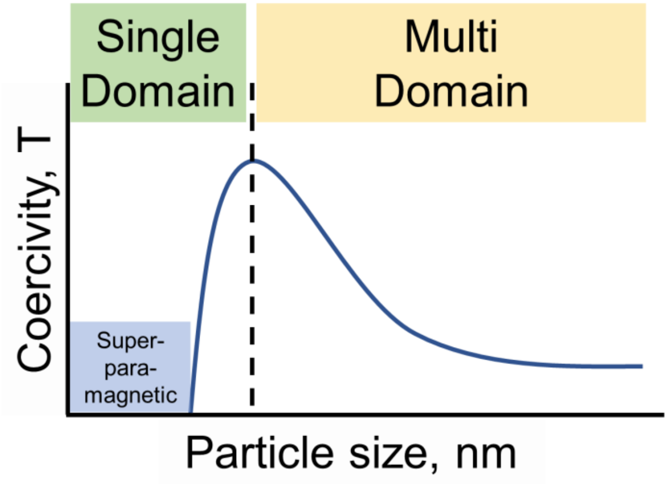

Figure 1.6 The change in coercivity as a function of particle size.

1.2.2 Blocking Temperature and Superparamagnetism

As a magnetic material is reduced down to the nanoscale it becomes more susceptible to thermal changes. This destabilizing effect on the magnetic ordering causes a decrease in the critical temperature, typically referred to as a blocking temperature, T_b. Above the blocking temperature, the magnetic nanoparticle shows superparamagnetism, i.e. complete reversibility of magnetization as a function of applied magnetic field. A material in the superparamagnetic state resembles the behavior of an ideal soft magnet by being able to reach M_s, but lacking any coercivity (Figure 1.7).

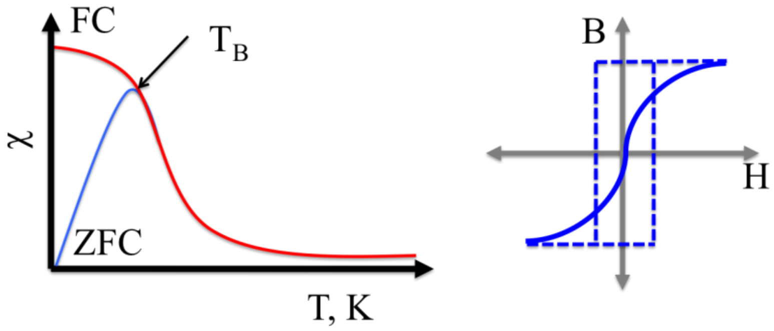

Figure 1.7 Left: the difference between the ZFC (blue) and FC (red) temperature-dependent magnetization of a nanomaterial. Right: the field-dependent magnetization of a material below (dashed line) and above (solid line) the blocking temperature.

The blocking temperature of a material can be established by measuring zero-field-cooled (ZFC) and field-cooled (FC) magnetization under applied direct current (DC) or alternate current (AC) magnetic field (Figure 1.7). In the temperature-dependent DC measurement, the divergence between the ZFC and FC curves occurs at T_b, while in the AC measurements the peak in the out-of-phase magnetization appears at T_b. Given the energy required for the spin in a magnet to realign are related to the anisotropy (K) and the volume (V), we can estimate the blocking temperature of a nanoparticle:

$$T_b = \frac{K_{eff}V}{25k_B} \tag{7}$$

assuming the probability for the spins to overcome the energy barrier is related to the Boltzmann constant (k_B).[11,13] Alternatively, we could also modify equation (7) to determine at what diameter (D) a particle will become superparamagnetic at a given temperature:

$$D = \sqrt[3]{\frac{31k_BT}{K_{eff}}} \tag{8}$$

From equation 8, a superparamagnetic size limit for a particle can be estimated for some target operational temperature. For instance, a $Nd_2Fe_{14}B$ smaller than 2.4 nm will be superparamagnetic at room temperature, given an anisotropy of 9.4 MJ/m^3.[14]

1.2.3 Shape Anisotropy

Due to the small scale of nanomaterials, magnetic anisotropy can be also achieved through changing the shape of the nanoparticle. By shaping a particle into a nanorod, the material gains a preferred magnetic alignment axis, which increases the coercivity. This effect applies even to soft magnets with cubic symmetry, where a 10:1 c/a ratio leads to a 12-fold increase in coercivity.[11] Nanoplates also exhibit the similar effect by making the in-plane magnetization strongly preferred.[15] Given the effect that surface area, volume, and shape have on the properties of magnetic materials, many nanocrystalline shapes have been studied for their effect on properties, including cubes, nanocacti, barbells, and wires.[16,17]

1.3 Magnetic Exchange Coupling

1.3.1 Exchange Spring Behavior

The exchange-spring effect occurs when two different ferro- or ferrimagnetic materials are layered onto one other, specifically at small thicknesses on the order of a several nanometers.[14,18] While the model involves a hard magnetic material being embedded into a soft magnetic material, any two ferro-/ferri- magnets can be mixed to produce varying degrees of exchange behavior. In an exchange-spring magnet, the benefits of hard and soft magnetic materials are combined, ideally generating a hard magnet that is higher saturation magnetization, thereby producing a larger energy product than the hard magnet could achieve on its own (Figure 1.8).

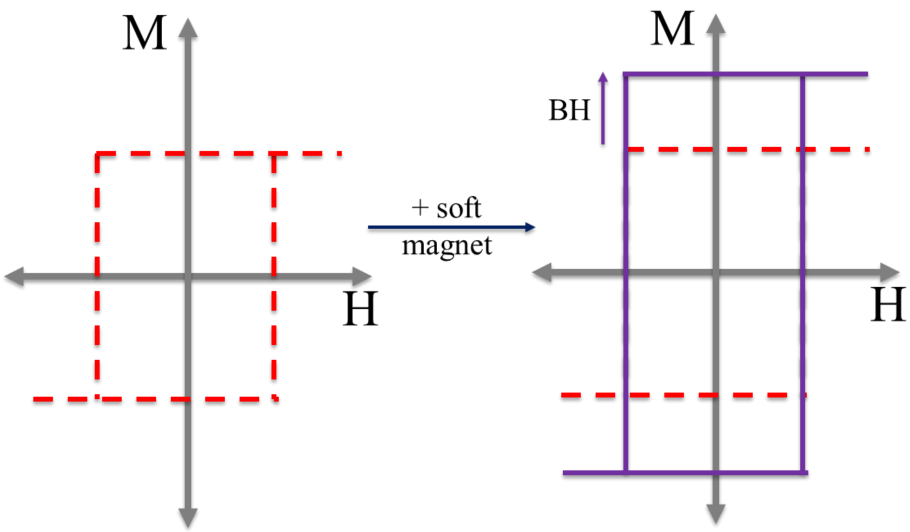

Figure 1.8 The energy product (BH) of a hard magnet (dashed red) can be increased by controllably mixing it with a soft magnet and generating an exchange-spring magnet (solid purple).

The "spring" part of the exchange-spring magnet signifies the higher susceptibility of the soft magnetic component to an applied field, allowing it to begin demagnetizing in relatively weak fields, The hard magnetic component, however, will not lose magnetization as quickly, so when the field is turned off, the original preserved alignment of the hard magnetic component will help to realign the soft magnetic component (Figure 1.9).[14] This means that the regions of recovery will be dictated by whether just the soft component is realigning or if the hard magnetic component is realigning as well. A balance needs to be maintained between adding enough of the soft component to increase the total remnant magnetization that can be recovered, with keeps the layer thin enough that it is still coupled with the hard magnetic component. When the soft component gets too thick, the outer most moments will no longer be coupled to the hard magnet, thus creating regions of non-recovery from the soft component having no means to realign with the core.

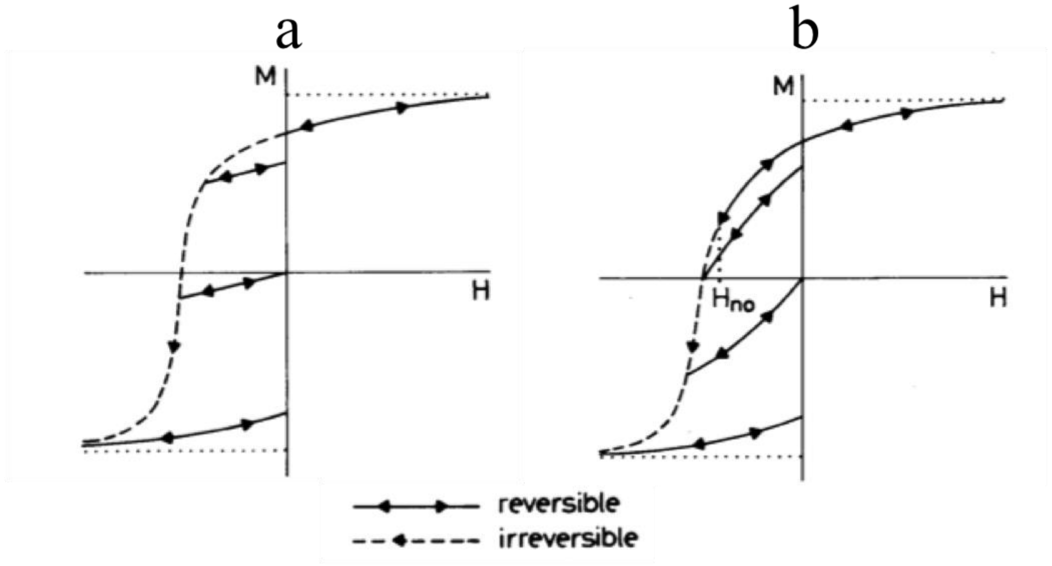

Figure 1.9 Differences in the demagnetization/remagnetization behavior between a conventional hard magnet (a) and an exchange spring magnet (b). © 1999 IEEE

1.3.2 Hard Exchange Coupling Behavior

While the exchange spring phenomenon occurs when a soft magnet is partially coupled to the hard magnet, another state can exist where the hard and soft components are perfectly coupled to one another. In this state, the total magnetic system will look like a stronger hard magnet with a larger saturation magnetization and larger coercivity. While the larger magnetization simply exists due to the higher M_s of the soft magnetic material, the enhanced coercivity is a somewhat unexpected result that can be explained in two ways. One explanation is the stabilizing effect that the shell may have on the surface spins of the core material, causing it to act like a larger magnetic system as compared to the unshelled material. The other explanation comes from the inherent coupling of moment and coercivity through anisotropy. The larger total magnetic magnetization is simply more difficult to rotate, which ultimately gives a larger coercivity.

1.3.3 Exchange Bias

Exchange bias is the result of layering an antiferromagnet onto a ferromagnet. This combination generates a material that shows a relaxation bias in a negatively applied field compared to a positively applied field (or vice-versa). This field dependent bias shifts the coercivity of the core material to be larger on one side of the hysteresis loop compared to the other, where in extreme cases the coercivity can be completely reduced to zero in one direction (Figure 1.10).

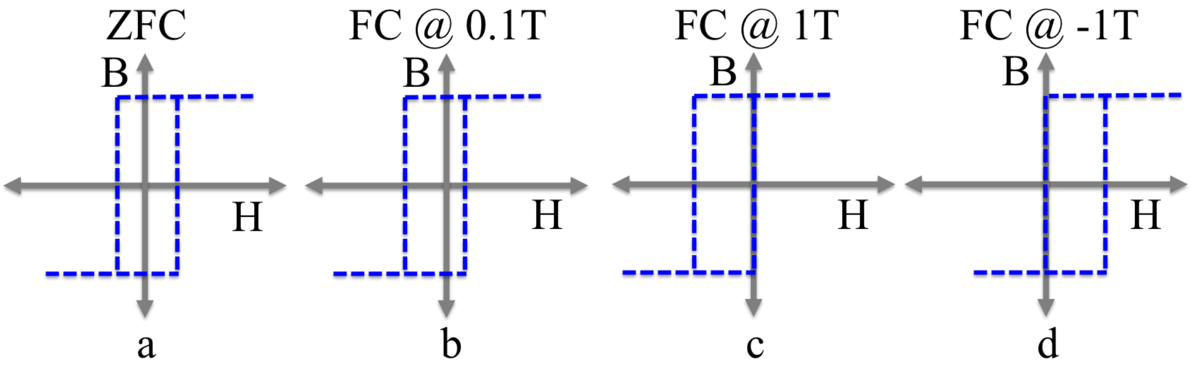

Figure 1.10 The role of cooling field in the behavior of an exchange bias material.

Changing the strength and direction of the applied field while cooling the system can control the extent of the bias. A stronger applied field will cause the antiferromagnetically coupled moments to be more aligned antiparallel to each other along the easy axis, thus generating a stronger bias effect on the ferromagnet. Likewise, magnetizing the bias material in a positive field will cause an increased coercivity when aligning the moments with a negative field and a decreased coercivity when applying a positive field during a field sweep. This happens because the moments at the interface of the two materials will align according to the applied cooling field. Since antiferromagnetically ordered moments will not realign with a changing field once they have aligned, a permanent interfacial bias is introduced, which influences the realignment of ferromagnetically coupled moments under the changing applied field.[19–22]

The exchange bias is an important effect that often allows identification of surface oxidation effects. While such oxidation in only a few interfacial layers might be undetectable by PXRD methods, exchange bias will be observed in magnetic measurements.

1.4 Generating Core@Shell Nanomaterials

1.4.1 Synthesis of Magnetic Cores

In order to study the complex magnetic behavior of exchange coupled materials, a core material must first be made. The standard process of generating magnetic nanoparticles is solvothermal decomposition and reduction of coordination complexes containing halide, acetylacetonate (acac), or carbonyl (CO) ligands.[16,23,24] Various solvents can be used depending on the desired reaction temperature, such as hexadecylamine (HDA, b.p. = 330°C) or dioctyl ether (DOE, b.p. = 285°C). The reduction process can be controlled by using such solvents as oleylamine (OAm, b.p. = 364 °C) or polyols which are known to assist in the reduction of transition metals. Other common solvents include octadecene (ODE, b.p. = 315 °C), which is useful as a non/weakly-coordinating solvent, oleic acid (OA, b.p. = 360), which is often using in conjunction with OAm in order to control coordination environment and shape growth, and trioctylphosphine/trioctylphosphineoxide (TOP/TOPO, b.p. = 290/212°C), which are used in similar fashion to OAm/OA but can introduce phosphorus into the nanostructure. Finally, in addition to using reducing solvents, long chain diols such as 1,2-hexadecanediol (b.p. = 356 °C) can serve as reducing agents.[25,26]

Single source precursors (SSP) also prove to be important in the synthesis of nanoparticles. These complexes can be used to control difficult reactions by taking advantage of having the relevant elements already bound to each other. Likewise, generating a SSP that has the correct ratio compared to the final product can facilitate the reaction, especially if the target elements have different reactivities when used as separate precursors.

1.4.2 Core@Shell materials

The most common way of shelling nanoparticles is through dropwise addition an appropriate metal coordination complex, either immediately after the formation of the core particles or after purifying and re-dispersing the core particles.[27–31] This process requires the core particles to be soluble, but the majority of hard magnetic nanoparticles require a high temperature annealing step (>600°C) at the end of the initial synthesis in order to achieve the target magnetic properties.[24,17,32,33] Such extra-processing step leads to burning out of all surface ligands, ultimately generating completely insoluble materials that cannot be redispersed in solution for shelling. Some hard magnetic materials that can be made without an annealing step include fcc-FePt[34], MnBi[35], and Fe_3Se_4[15], but these materials do not possess sufficiently high performance characteristics to replace current state-of-the-art magnets. It also should be mentioned that magnetic oxide shell, can be generated by controlled surface oxidation of a preformed core material. Such approach, for example, was used to form Co@CoO exchange-biased particles.[21]

1.4.3 Epitaxial Growth

An important aspect of growing a shell onto a particle is ensuring that the two materials are structurally compatible. If the lattice constants of materials are too different from one another, the amount of strain generated in the system will prevent the formation of regular interface between the core and shell structures. When two materials have identical structures, the interface can be formed without appreciable strain, which is known as epitaxial growth.[36–38]

1.5 Microwave Reactors

1.5.1 Selective Heating

While microwaves are praised for promoting fast chemical reactions, a major benefit to microwave synthesis is the selective heating that can occur when proper precursor/solvents are selected.[39–41] If a low microwave absorbing solvent is used with a high cross-section precursor, then the heating can occur directly at the target, allowing for rapid reactions.[42] The heating can also change over the course of the reaction as metallic particles grow and become better microwave absorbers than the solvent molecules. Controlling the selectivity of the microwave heating can allow for several benefits, including faster reactions, increased reaction efficiency, and better control of the product formation.[43] It also has been shown that the effects from the microwave coupling to the magnetism of particles contribute far less to the overall heating than the effects of the particle size.[44]

A serious issue that arises from microwave heating is the potential for thermal runaway, i.e. the situation when the metallic particles grow large enough to become so rapidly heated in the microwave that the reaction goes out of control. Because the metallic particles can heat to temperatures that are higher than the solvent boiling point, a chain reaction will occur causing rapid solvent evaporation, condensation of metal particles, and overheating, which can lead to dramatic and hazardous consequences. Therefore, it is important to ensure that the materials used in the reaction are sufficiently soluble in the solvents or that low enough concentrations are used to ensure that the amount of generated heat can be reasonably contained and the reaction can remain under control at all times.

1.6 Research Objectives

The review of the state of the knowledge in the areas of magnetic nanoparticles and permanent-magnet materials allows the formulation of research objectives to be pursued in this dissertation:

1. Investigation of how the exchange properties will change in the case of an increasing soft magnetic shell on a hard magnetic core. Chapter 3 will exhibit how the magnetic properties of a 5 nm fcc-FePt nanoparticle change with the gradual addition of an ε-/fcc-Co shell. These particles will be made in a microwave reactor and shelled through drop-wise addition under continual microwave irradiation. The different exchange regimes will be observed as well as their corresponding effects on M_s, H_c, and %recovery.
2. In chapter 4, additional FePt core sizes with varying shell thicknesses will be investigated to determine if and how the hard magnet affects exchange. Using 3, 5, and 7 nm fcc-FePt cores, a systematic application of similar cobalt shell thicknesses across all three core systems will generate a clear trend in exchange behavior. From this work, it will become clear what roles the hard and soft components play in the magnetic properties and exchange limits of a core@shell system.
3. Chapter 5 will look at how changing the actual soft magnet used will alter the exchange limits in the core@shell system. By applying a fcc-Ni shell to a 5 nm fcc-

FePt core, the effects of having a core@shell system with mismatched unit cell and magnetocrystalline anisotropy will be explored. The analysis of the resulting M_s and H_c with an evolving shell will clearly show the inhibiting effects that the two magnetic systems will have on one another.

4. In chapter 6, alternative hard magnetic nanoparticles will be synthesized and explored for their potential use in a core@shell system. Microwave syntheses of $SmCo_5$ and Fe_3Se_4 nanoparticles will be developed and their resulting magnetic properties will be studied. Given the concerns of oxidation and byproducts with the use of Se powder and $Fe(acac)_3$ as precursors, it was instead determined that Ph_2Se_2 and $Fe_3(CO)_{12}$ would be a better for both the microwave and conventional heating methods.

CHAPTER 2

MATERIALS AND METHODS

2.1 Starting Materials

The powders Pt(acac)$_2$ (97%), Fe$_3$(CO)$_{12}$ (with 1-10% MeOH), Fe(acac)$_3$ (97%), Co(acac)$_2$ (97%), and Ni(acac)2 were purchased from Sigma-Aldrich and used without further purification. The solvents Oleylamine (70%), Oleic Acid (90%), Dioctyl ether (99%), and benzyl ether (98%) were purchased from Sigma-Aldrich and were used without further purification. All reactions were degassed after mixing the precursors and then performed under N2 in either a Schlenk flask or a sealed microwave tube.

2.2 Synthesis

All core materials were made using solvothermal methods in either a Schlenk flask and heating mantel or in a CEM microwave reactor. Shelling of the particles was performed in a CEM microwave through means of slow addition of the appropriate shelling material. All materials were isolated by addition of toluene to the mixture followed by drop wise addition of MeOH to precipitate the particles, followed by centrifugation. The isolated solid residue was washed repeatedly with toluene and MeOH followed by centrifugation until the supernatant became clear and colorless. Final purification was achieved by magnetic separation instead of centrifugation. The sample was collected by removal of the supernatant and dried under vacuum.

2.2.1 Synthesis of 3.4 nm FePt particles

A stock solution of 1 mmol of Pt(acac)$_2$ in 10 mL of oleylamine/oleic acid (6:1 v/v) was prepared and degassed under vacuum at 60 °C until it turned dark yellow. The reaction vessel was placed under N_2 and 3 mmol of 1,2-hexadecanediol (hdd) was added. Once the hdd dissolved completely, 0.66 mmol of $Fe_3(CO)_{12}$ was added, generating a deep red solution.

The FePt nanoparticles were synthesized by syringing 2 mL of the stock solution into an 8 mL Pyrex® microwave reactor vessel under N_2. The vessel was heated to 150 °C for 5 min in a microwave reactor (CEM Explorer, 2.45 GHz, 300 W) maintaining constant temperature via active cooling.

2.2.2 Synthesis of 4.9 nm FePt particles

A stock solution of 1 mmol of $Pt(acac)_2$ in 10 mL of oleylamine/oleic acid (4:1 v/v) was prepared and degassed under vacuum at 60 °C until it turned dark yellow. The reaction vessel was placed under N_2 and 3 mmol of 1,2-hexadecanediol (hdd) was added. Once the hdd dissolved completely, 0.66 mmol of $Fe_3(CO)_{12}$ was added, generating a deep red solution.

The FePt nanoparticles were synthesized by syringing 2 mL of the stock solution into an 8 mL Pyrex® microwave reactor vessel under N_2. The vessel was heated to 150 °C for 5 min in a microwave reactor (CEM Explorer, 2.45 GHz, 300 W) maintaining constant temperature via active cooling.

2.2.3 Synthesis of 7.3 nm FePt particles

A stock solution of 1.0 mmol of $Pt(acac)_2$ in 15 mL of oleylamine/oleic acid (4:1 v/v) was prepared and degassed under vacuum at 60 °C until it turned dark yellow. The reaction vessel was placed under N_2 and 3 mmol of 1,2-hexadecanediol (hdd) was added. Once the hdd dissolved completely, 0.66 mmol of $Fe_3(CO)_{12}$ was added, generating a deep red solution.

The FePt nanoparticles were synthesized by syringing 3 mL of the stock solution into an 8 mL Pyrex® microwave reactor vessel under N_2. The vessel was heated to 150 °C for 5 min in a microwave reactor (CEM Explorer, 2.45 GHz, 300 W) maintaining constant temperature via active cooling.

2.2.4 Preparation of 0.2M Co shelling solution

Using a 100mL Schlenk flask, 2mmol of $Co(acac)_2$ was dissolved in 8mL of oleylamine and 2 mL of oleic acid. This solution was degassed at ~80°C for ~1 hour and placed back under N_2, the flask was evacuated 2 more times and placed back under N_2 in order to ensure an inert atmosphere.

2.2.5 Preparation of 0.2M Ni shelling solution

Using a 100mL Schlenk flask, 2mmol of $Ni(acac)_2$ was dissolved in 8mL of oleylamine and 2 mL of oleic acid. This solution was degassed at ~80°C for ~1 hour and placed back under N_2, the flask was evacuated 2 more times and placed back under N_2 in order to ensure an inert atmosphere.

2.2.6 Shelling FePt cores

After the cores are formed in the microwave (5 minutes in), the reaction was continued so that they were shelled in-situ. An initial injection of 0.5-1mL of shelling solution was injected with a syringe to ensure all of the FePt cores had at least one layer of the shell formed on each particle. After the initial injection, a syringe pump could be used to add the Co or Ni shelling solution at a rate of 0.5mL/min. In order to ensure the reaction was complete at the end, it was allowed to continue for another 2.5 minutes from the time the last addition was administered. The size of the shell was controlled by the amount of solution added over time.

2.2.7 Microwave synthesis of Fe_3Se_4 nanoparticles

To 10mL of Oleylamine, 2mmol of diphenyl diselenide and 1mmol of 1,2-hdd were added and degassed for 30 minutes. After evacuating the chamber and refilling with N_2 two more times, 1mmol of triiron dodecacarbonyl and the vessel was quickly degassed and refilled with N_2

one more time. From this bulk solution, 2mL aliquots were put into 6 mL Pyrex® microwave reactor vessel under N_2. The vessel was heated to 100°C for 5 min in a microwave reactor (CEM Explorer, 2.45 GHz, 300 W) and then further heated to 280°C for another 10 minutes maintaining constant temperature at both temperature points via active cooling. At the end of the reaction, the microwaves were turned off and the sample was cooled using air.

2.2.8 Microwave synthesis of $SmCo_5$ nanoparticles

To 20mL mixture of Oleylamine/Oleic acid (4:1 v/v), 4mmol of $CoCl_2$, 2mmol of $Sm(NO_3)_3$and 1mmol of 1,2-hdd were added and degassed for 30 minutes. After evacuating the chamber and refilling with N_2 two more times. From this bulk solution, 10 mL aliquots were put into a 40mL quartz pressure vessel under N_2. The vessel was heated to 280°C for 10 min in a microwave reactor (CEM Explorer, 2.45 GHz, 300 W). At the end of the reaction, the microwaves were turned off and the sample was cooled using air.

2.3 Physical Measurements

2.3.1 X-ray diffraction

Room temperature powder X-ray diffraction was performed on the Rigaku Ultima III diffractometer equipped with a Cu-Kα source, a micro area sample stage, and a CCD detector. Data were collected at room temperature, in the 2θ range of 10-80° over the course of 30 minutes.

2.3.2 Infrared spectroscopy

Infrared (IR) spectroscopy was performed on a PerkinElmer Spectrum 100 FT-IR spectrometer. The particles were mixed with a minimal amount of KBr and analyzed as solid samples.

2.3.3 Inductively-coupled plasma mass spectrometry

ICP-MS was used to determine the metal content of the nanoparticles using an Agilent 7500cs single collector quadrupole ICPMS instrument. The samples were dissolved in HNO_3 and run in the system at 1500W.

2.3.4 Thermal gravimetric analysis

TGA was performed using a Q600 thermal analyzer (TA Instruments) in order to determine the ligand content of the particles. Measurements were performed in the range of 30-900 °C at a heating rate of 5 °C/min.

2.3.5 Transmission electron microscopy

TEM images were recorded using a JEM-ARM200cF electron microscope at 200 kV accelerating voltage. The samples were dropcast from dispersion in toluene onto a 200 mesh copper grids and left to dry under reduced pressure overnight.

2.3.6 Magnetic measurements

Magnetic measurements were performed on a MPMS-XL (Quantum Design). Samples were placed in a gelatin capsule and covered with 1-eicosene wax to prevent reorientation of particles under magnetic field during the measurements. Zero-field-cooled (ZFC) and field-cooled (FC) magnetization was measured in a constant applied magnetic field of 10 mT. Field-dependent magnetization was measured at 5 K, with the applied field varying from –5 to 5 T. All values obtained were corrected by accounting for the mass content of the surface-passivating ligands. Magnetization recovery was studied by applying a fixed demagnetizing field, then turning it off and registering the recovered magnetization value. This procedure was repeated with increasingly stronger demagnetizing fields until the coercive point had been passed. The magnetization recovery values (η) reported below correspond to the magnetization recovered after the coercive point was reached and the field was turned off.

Energy product calculations were performed by converting the measured magnetization values from emu/g (cm3/g) to Gauss. After subtracting the ligand contribution to the mass of the samples, the established core-shell compositions (Table 1) and the know densities of the bulk materials were used to convert magnetization values from emu/g to emu/cm3. By multiplying the emu/cm3 by 4π, the values were converted to Gauss.

CHAPTER 3

EVOLUTION OF EXCHANGE COUPLING BEHAVIOR IN 5 NM FEPT PARTICLES WITH VARIABLE COBALT SHELL THICKNESSES

3.1 Introduction

High performance magnets are critical components in energy technologies for rotors and magnetic bearings in motors. Growing awareness of economic limitations associated with rare-earth containing materials has stimulated innovative research efforts to replace rare-earth based magnets with more sustainable alternatives.[7,35,45,46] Consequently, a grand challenge for energy applications of magnetic materials is the development of controlled architectures of nanoscale magnetic composites that outperform current technologies by reducing rare-earth content while affording comparable or larger energy products. Current energy needs require magnets that are capable of maintaining coercivities of 0.5 to 2 T at elevated temperatures. In order to meet these requirements, current magnets incorporate rare-earth metals, such as $Nd_2Fe_{14}B$, that result in energy products >60 MGOe.[47] It has been postulated that patterned nanocomposites consisting of hard and soft magnetic domains can achieve a 6-fold improvement in energy product over the simple hard magnet due to magnetic exchange behavior at the nanoscale.[48] Assembled in a controlled fashion, such nanocomposites will offer an opportunity to alter the approach to high-performance magnet design by reducing rare earth content, enhancing remnance without lowering coercivity, and allowing facile composite manufacturing. It is the controlled assembly, however, that is currently lacking in the study of such hard-soft magnetic composites. While multilayer films of hard and soft magnets have been successfully demonstrated and extensively investigated,[36,49,50] achieving the same level of control at the nanoparticle scale has proven to be challenging, with only a handful of successful approaches reported in the literature.[51,27,52]

We demonstrate the synthesis of $Fe_{0.65}Pt_{0.35}$@Co nanomagnets by one-pot microwave (MW) chemistry methods. The Co shell of variable thickness was grown onto 4.9+0.6 nm fcc-$Fe_{0.65}Pt_{0.35}$ core. As the shell thickness increases, the predicted evolution from hard-coupled to exchange-spring and finally to beyond exchange-coupled behavior in the hard-soft nanocomposite is observed for the first time. Correlating the change in saturation magnetization (M_{sat}), coercivity (H_c), remnant magnetization recovery (η), and energy product (BH) across the observed magnetic regimes results in a surprising observation, namely, at shell thicknesses ≤1 nm, the core-shell nanostructure provides an unexpected doubling of the coercivity, generating a dramatic enhancement in the energy product from 1.1 MGOe for the bare $Fe_{0.65}Pt_{0.35}$ nanoparticles to 3.8 MGOe for the $Fe_{0.65}Pt_{0.35}$@Co nanocomposite. By increasing the shell thickness to 1.7 nm, the exchange-spring effect is maximized, resulting in a remnant magnetization recovery of $\eta = 75\%$ from the coercive point. Loss of exchange spring behavior is observed as the Co layer grows thicker due to the decoupling of the outermost layers soft-magnet layers from the hard-magnet core.

We emphasize that the fcc-$Fe_{0.65}Pt_{0.35}$@Co core-shell nanomagnet described in this study represents the first synthetic model system to interrogate the onset of exchange-spring behavior and not a material for direct energy applications, although rather high coercivity of 0.575 T was observed. The choice of the fcc-FePt as a model hard core avoids the diffusion of Co into the particle core that could take place during the thermal treatment needed to produce magnetically harder face-centered tetragonal (fct) FePt. We also note the current interest in potential biomedical applications of FePt nanoparticles.[53,54]

Kneller and Hawig coined the idea of exchange-spring magnets, based upon the earlier suggestion by Goto that the exchange interaction between the hard and soft magnetic layers results in a helical arrangement of moments in the soft layer over twice the domain wall width.[14,55] Skomski and Coey theoretically showed energy products could be increased by 6-fold for a $Sm_2Fe_{17}N_3$ (hard)-FeCo (soft) ordered composite.[48] In order to achieve the highest performance in colloidal nanocomposites, a soft magnet with a large saturation magnetization should be coupled with a hard magnet with a large coercivity. The preparation of hard-soft magnetic nanocomposites has been performed by both mechanical and chemical methods. Ball-milling is one of the most commonly used mechanical approaches, but it leads to grain boundaries and irregularities in the final materials, resulting in rather insignificant, if any, enhancement of the energy product.[56–59] In contrast, chemical approaches often require an intermediate annealing step to make the hard component, causing issues with controlling size dispersion as well as making it difficult to get the nanoparticles back into solution.[27,51]

Sun et al. have achieved the most significant results to date through the use of colloidal synthetic approaches based upon successive ionic layer adsorption and reaction (SILAR) to prepare a series of hard-soft core@shell materials that consisted of 4 to 9.5 nm thick Co shells (soft magnet) on 8 nm face-centered tetragonal (fct) FePt particles (hard magnet). The isolated materials, however, did not exhibit the enhanced energy product expected from the theoretical models; the loss of coercivity was observed with increasing shell thickness.[60] While the idea of exchange-spring behavior in core@shell nanomagnets has been purported, the observation of the evolution from hard-coupled to exchange-spring behavior in hard-soft nanomagnet composites, as the shell layer grows, still awaits experimental confirmation, reflecting the difficulty to control structural order and shape in nanoscale magnets.

3.2 Results and Discussion

3.2.1 Core Synthesis and Shelling

The SILAR protocol was adapted to a MW reactor through the use of high-temperature reduction of the molecular precursors $Pt(acac)_2$, $Fe_3(CO)_{12}$, and $Co(acac)_2$ in oleylamine/oleic acid, carried out under a N_2 atmosphere. Nucleation of the core within the MW cavity (CEM Explorer, 2.45 GHz, 300 W) was achieved at 150 °C within 5 minutes, producing the spherical 4.9+0.6 nm FePt nanoparticles (Figure 3.1). This process reflects the known efficiency for nanoparticle formation in a MW reactor due to rapid nucleation through efficient volumetric heating of the oleic acid/oleylamine solvent mixture coupled to La Mer limited growth of the core during the short reaction times.[42,43]

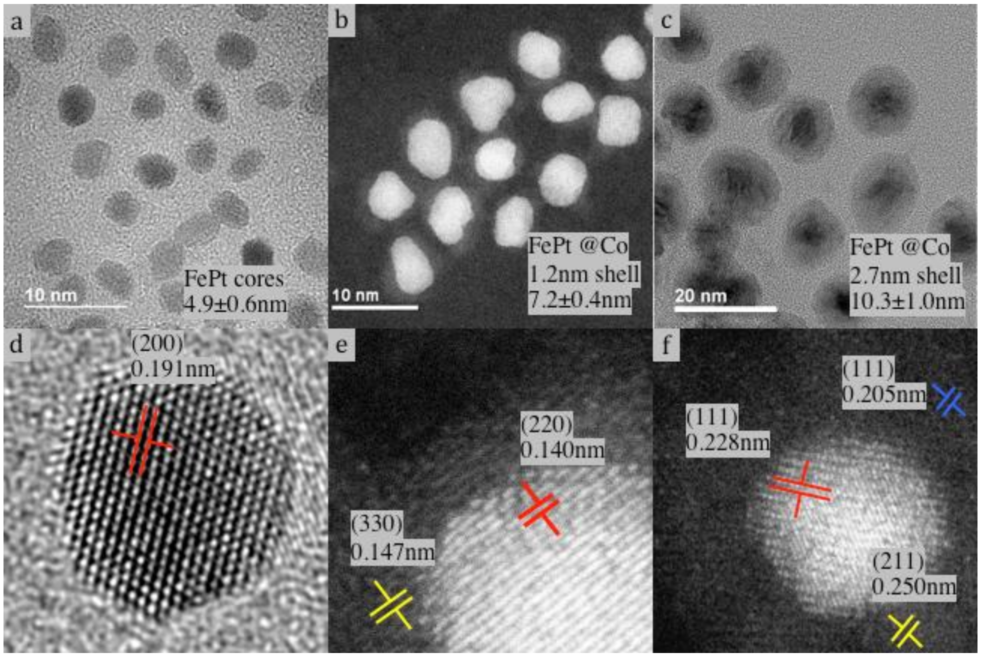

Figure 3.1 HR-TEM images of the Fe0.65Pt0.35 cores (a, d) and the core-shell nanoparticles with the 1.2 nm (b, e) and the 2.7 nm (c, f) Co shell.

The formation of FePt nanoparticles was followed by addition of the Co precursor at 150-160 °C, leading to growth of a Co shell (0.6 nm to 2.7 nm; Figures 3.1b and 3.1c). When the same reaction conditions were applied to the pure solution of Co(acac)$_2$, in the absence of the Pt and Fe precursors, we observed the formation of Co particles only at temperatures exceeding 240 °C. These observations suggest that the FePt cores serve as local "hot spots", at which the deposition of the Co shell takes place, while the average temperature of the reaction medium does not allow the nucleation of pure Co nanoparticles.[35]

Table 3.1 The metal content in of the FePt and FePt@Co nanoparticles as determined from the ICP-MS analysis.

Co shell thickness, nm	Core composition, mol. %		Core/shell composition, mol. %		
	Fe	Pt	Fe	Pt	Co
0	65±0.4	35±1.0	65±0.4	35±1.0	0
0.6	65±0.7	35±0.8	47±0.5	25±0.6	27±0.5
1.0	64±1.0	36±1.3	40±0.6	23±0.8	37±0.7
1.2	66±3.0	34±2.9	29±1.3	15±1.3	56±1.2
1.7	68±1.6	32±1.0	25±0.6	13±0.4	62±0.6
2.0	65±4.0	35±2.8	18±1.1	10±0.8	72±0.9
2.3	60±4.5	40±3.2	8±0.6	5±0.4	87±0.5

TEM images revealed the formation of distinct nanocrystals of narrow dispersity (Figure 3.2), with no evidence of phase-segregated FePt or Co nanocrystals or Janus-type composites. ICP-MS measurements of the nanocrystals established the Fe:Pt ratio of ~65:35 for all samples (Table 3.1). The isolated core@shell nanocomposite was passivated by a mix of acetylacetonate, oleylamine, and oleic acid, as confirmed by characteristic bands observed in FT-IR spectra (Figure 3.3). The ligand content was determined from TGA measurements that indicated ligand loss equivalent to ~31(2) wt.% of the core@shell nanocomposite (Figure 3.5).

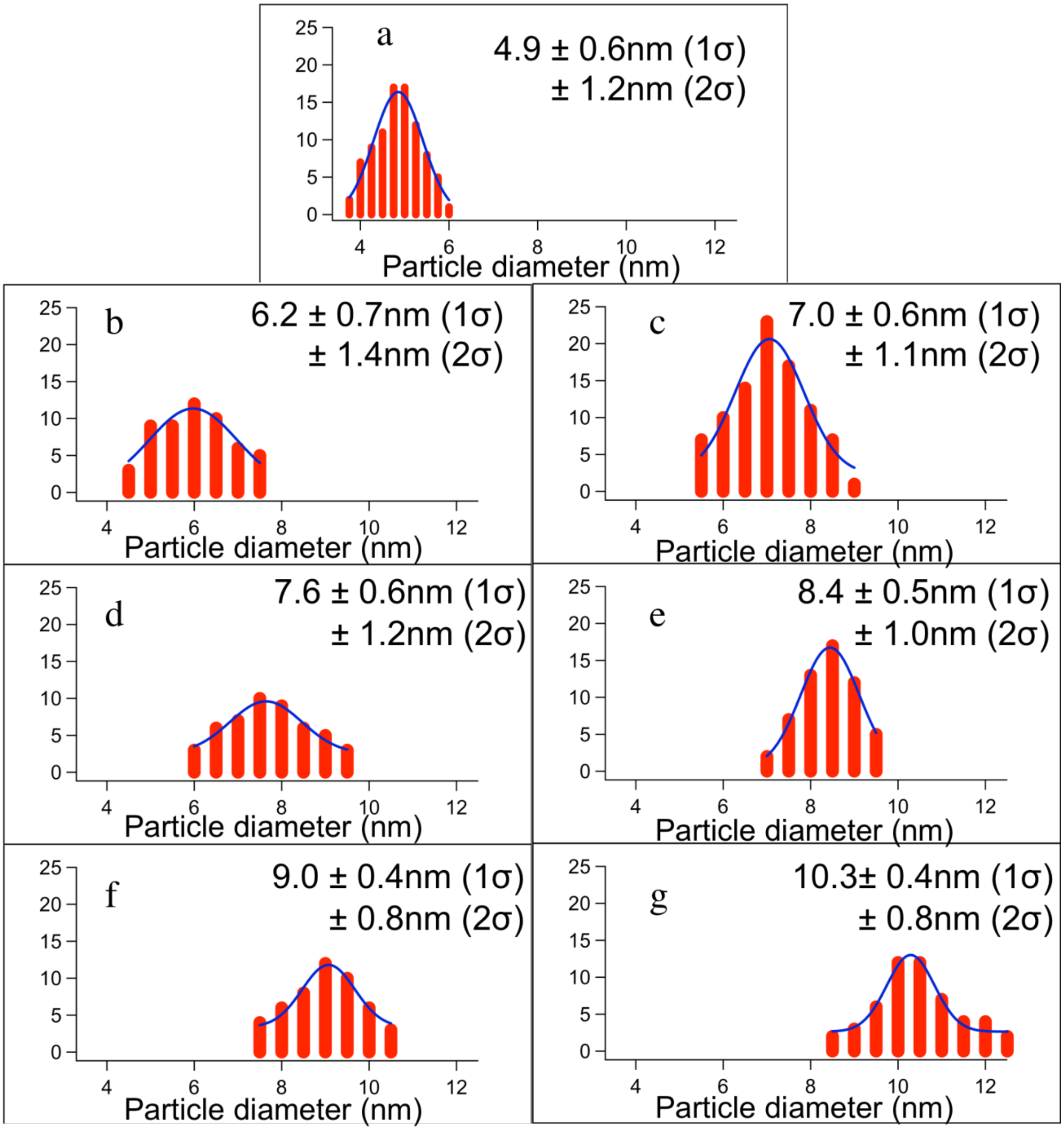

Figure 3.2 Size histograms measured for FePt/Co core-shell nanoparticles with the (a) 0 nm, (b) 0.6 nm, (c) 1.0 nm, (d) 1.2 nm, (e) 1.7 nm, (f) 2.0 nm, and (g) 2.7 nm thick Co shells.

The use of oleylamine/oleic acid solvent mixture, rather than only oleylamine, enhances MW absorption by the reaction medium to afford rapid volumetric heating of the reaction mixture, uniform nucleation, and rapid depletion of the monomer concentrations to achieve size focusing, as previously reported for metal chalcogenide nanocrystals grown in a MW reactor.[42,43] The enhanced MW absorption from the 4:1 oleylamine/oleic acid solvent mixture is demonstrated by high-frequency dielectric spectroscopy (Figure 3.4). We did not observe decomposition of metal-acac precursors to oxides under the reaction conditions, which reflects the lower reaction temperatures and the reducing environment.

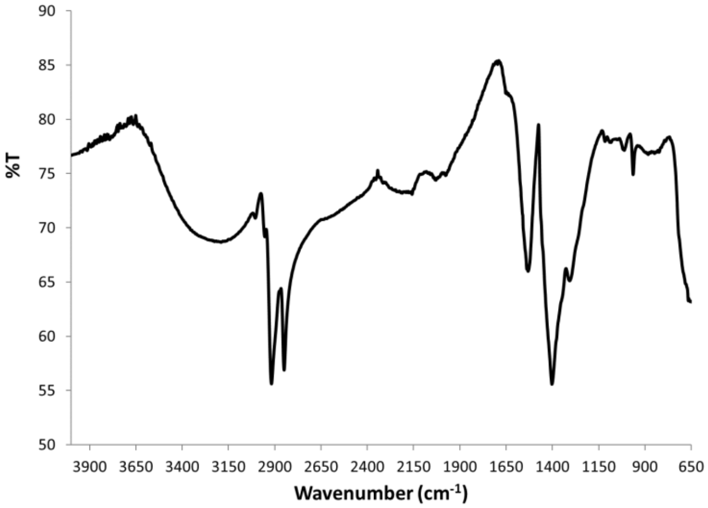

Figure 3.3 IR spectrum of 4.9 nm FePt.

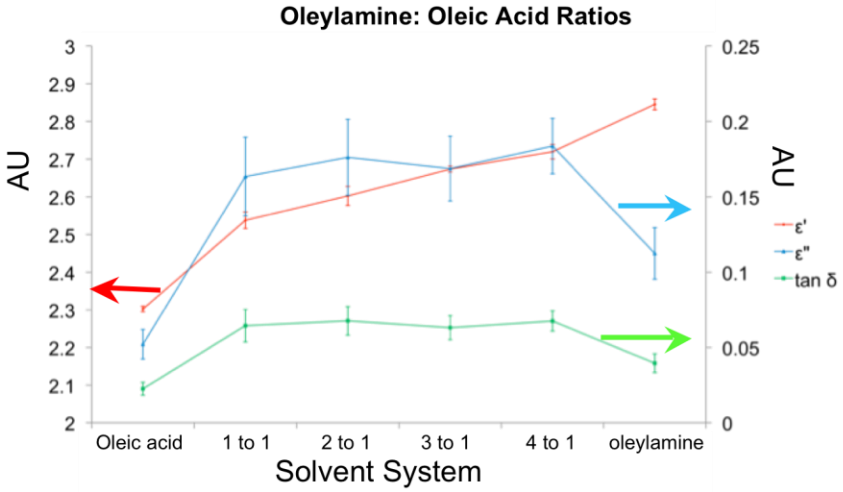

Figure 3.4 Dielectric spectroscopy of oleylamine/oleic acid mixtures.

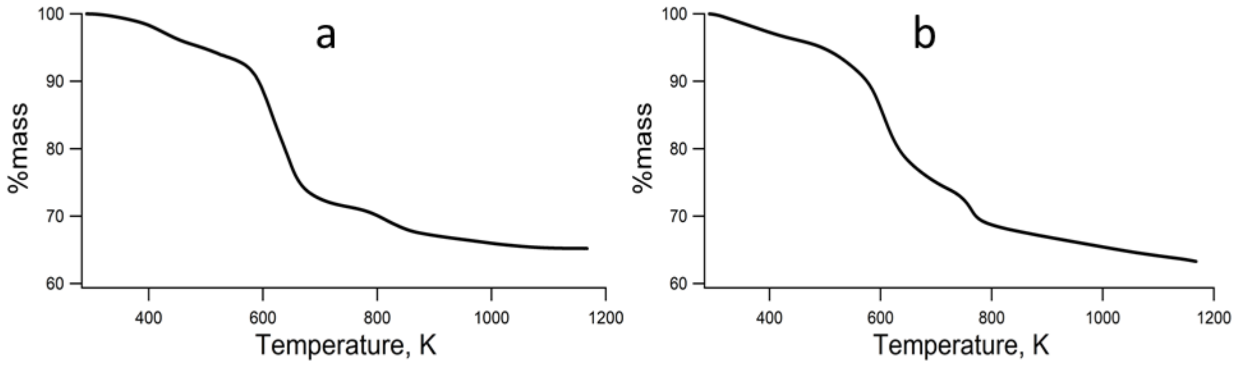

Figure 3.5 TGA curves measured on the $Fe_{0.65}Pt_{0.35}$ cores (a) and the $Fe_{0.65}Pt_{0.35}$@Co nanoparticles with a 1nm thick Co shell (b).

3.2.2 Structure characterization

The structure of the FePt and FePt@Co nanocrystals was analyzed by measuring the lattice fringes in high-resolution TEM images (HR-TEM). The phase assignments were supported by pXRD, which showed that the core is comprised of fcc-FePt (Figure 3.7), which was confirmed by identifying the corresponding (200), (220), and (111) lattice planes in the TEM images (Figure 3.1b). Assignment of lattice fringes for the 1.2 nm Co shell suggests the metastable ε-Co (330) plane growing onto the fcc-FePt (220) plane (Figure 3.1d).

Indexing lattice planes for thicker Co shells (e.g., 2.7 nm) showed that the ε-Co phase relaxed to adopt the fcc-Co structure in the outer shells, resulting in the appearance of both the (211) ε-Co and (111) fcc-Co lattice planes in Figure 3.1f. No change in the size or structure of the FePt cores was observed in the TEM images for all Co shell thicknesses. Both the ε- and fcc-type structures have been reported for lyothermally grown Co nanoparticles,[61] but only the fcc structure has been reported for thick Co shells grown on FePt.

The pXRD confirmed the formation of fcc-FePt cores (Figure 3.6). The presence of Co could not be observed in the pXRD patterns until the Co shell thickness reached 1.7 nm.

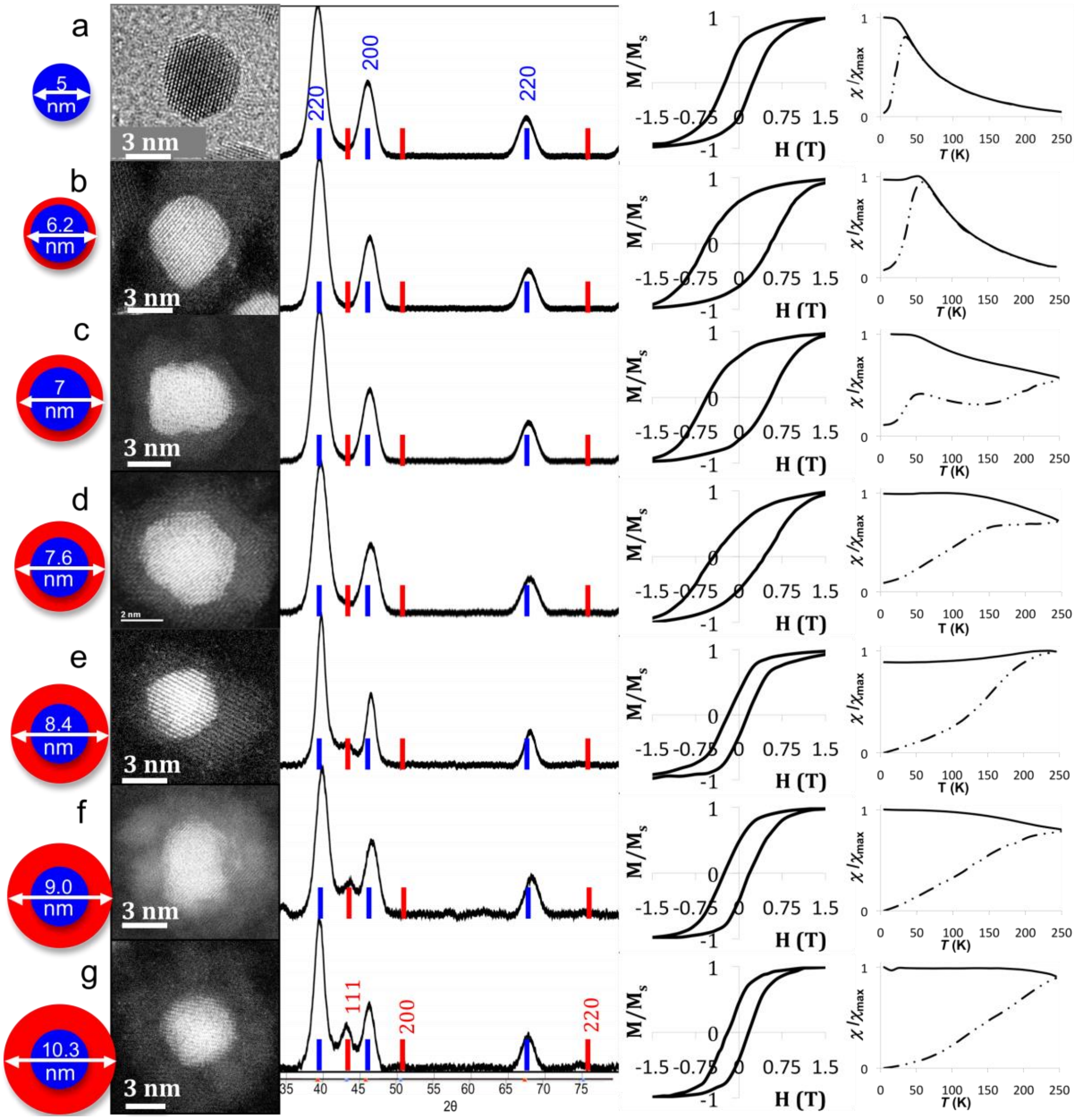

Figure 3.6 From left to right: pictograms, HR-TEM images, pXRD patterns, isothermal (5 K) hysteresis loops, and isofield (10 mT) ZFC-FC magnetization curves of the fcc-FePt/Co core/shell nanoparticles, in the order of increasing Co shell thickness: (a) 0 nm, (b) 0.6 nm, (c) 1.0 nm, (d) 1.2 nm, (e) 1.7 nm, (f) 2.0 nm and, (g) 2.7 nm.

Nevertheless, a progressive shift of the (200) pXRD reflection of FePt to higher 2θ angles suggests increasing strain in the core-shell architecture for the thicker Co shells. Thus, we believe the observation of the metastable ε-Co phase for shell thicknesses below 1.7 nm reflects interfacial strain and fast crystallization conditions, which lead to the less regular arrangement of Co atoms. Consistent with these arguments, the Co lattice is observed to relax to the fcc structure for the thickest Co shells.

The MW-assisted SILAR method allows deposition of Co shells onto pre-formed, uniformly sized FePt cores, avoiding phase segregation of individual Co and FePt components. The growth of the Co shell occurs in a nearly monolayer fashion, which has not been previously observed. This phenomenon can be explained by the fact that the 150 °C reaction temperature for Co shelling is much lower than the 240 °C solvent temperature required to nucleate individual Co nanoparticles. Thus, the MW is speculated to selectively heat the already formed cores instead of heating the surrounding solvent.

The proposed mechanism of surface-activated Co formation due to MW interaction with the FePt cores is supported by results from dielectric spectroscopy performed on the FePt core nanoparticles as compared to the pure oleylamine/oleic acid solvent (Figure 3.7). The dielectric spectroscopy shows enhanced MW interaction and absorption (imaginary component of the complex dielectric and tangent delta) relative to that of the solvent. This enhanced MW interaction indicates superheating of the FePt surfaces, which likely leads to the Co growth onto the FePt nanoparticles.[62] The increased absorptivity is consistent with literature results from studies on catalytic activity enhancement on magnetic nanomaterial surfaces due to surface heating in the MW field arising from ohmic and induction losses.[63–65]

Attempts to achieve the same level of control for shelling in a traditional SILAR lyothermal reaction produced non-uniform materials for reactions carried out between 150 °C and 250 °C (Figure 3.7). Indeed, Sun et al. reported that shelling required temperatures over 300 °C in the synthesis of FePt@Co core-shell materials using conventional heating.[66]

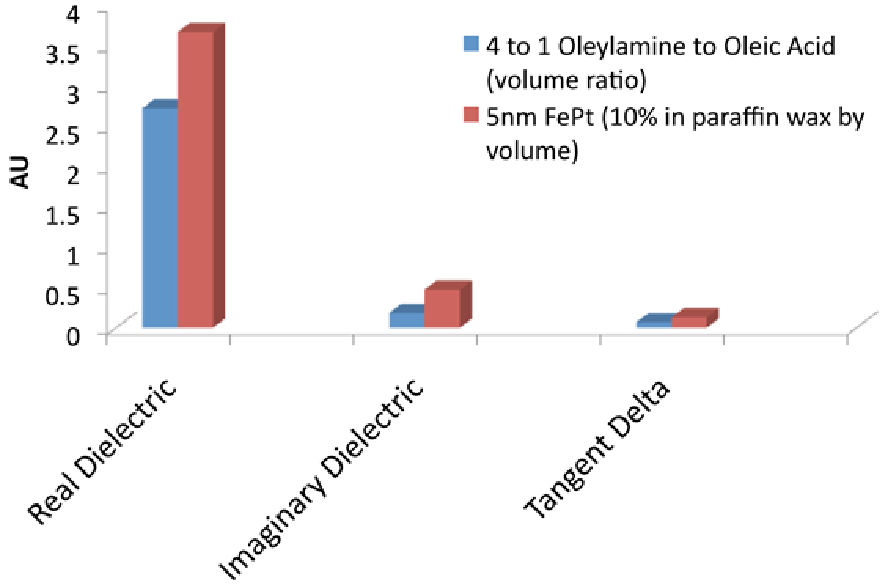

Figure 3.7 Dielectric spectroscopy comparing the microwave permittivity of the solvent and the 5nm FePt particles.

3.2.3 Magnetic Properties

The evolution of magnetic behavior of nanocomposites was studied via magnetization measurements performed on the FePt and FePt@Co samples immobilized in 1-eicosane. The divergence of ZFC and FC temperature dependent magnetization curves indicates that the 5-nm FePt core behaves as a superparamagnet with blocking temperature (TB) of 35 K (Figure 3.6a). The field-dependent magnetization sweep performed at 5 K revealed a sizable hysteresis, with H_c= 0.25 T and M_{sat}= 20 emu/g after subtracting the ligand mass contribution. The observed T_B, H_c, and Msat values for the FePt core are consistent with values reported for fcc-FePt nanoparticles in this size range.[67]

The addition of the first Co shell (rCo = 0.6 nm) led to the increase in T_B to 55 K (Figure 3.7b). For thicker Co shells, however, the T_B values exceeded 250 K (Figures 3.6c-g). This dramatic increase in T_B can be explained by the Co shell exceeding the characteristic correlation length above which the blocking of the particle's magnetization can be observed. Thus, while the magnetism blocking at r_{Co} = 0.6 nm is dictated by the properties of the FePt core, at $r_{Co} \geq 1$ nm it depends on the properties of the Co shell, as the higher TB is in agreement with the much higher Curie temperature of bulk Co (1400 K) as compared to bulk fcc-$Fe_{0.65}Pt_{0.35}$ (710 K).[68] For instance, in the case of the 7.6-nm FePt@Co nanoparticles with r_{Co} = 1.3 nm (Figure 3.6d), the T_B value exceeds substantially the one reported for the fcc-FePt nanoparticles of comparable size (TB ≈ 75 K at 8 nm).[69]

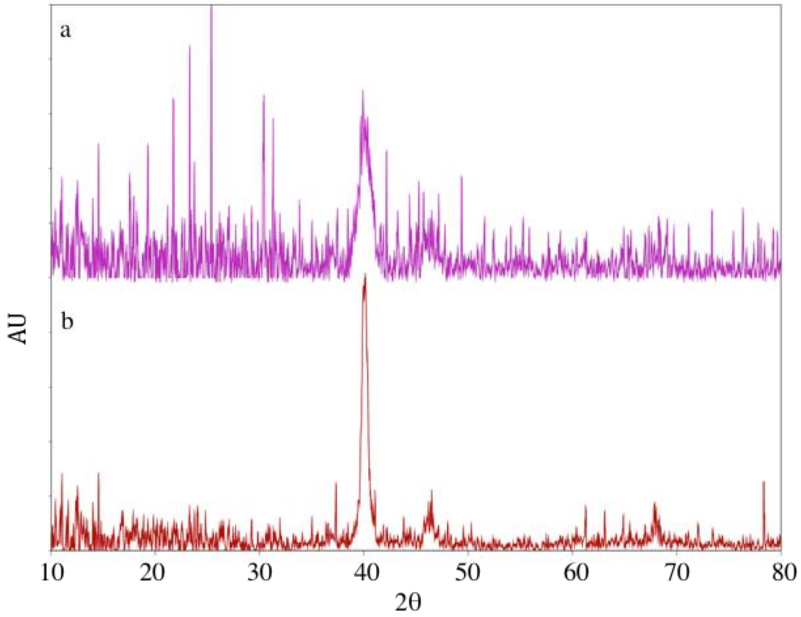

Figure 3.8 Powder X-ray diffraction patterns of reaction products after attempts to obtain FePt/Co core-shell nanoparticles in a round bottom vessel at 300°C (a) and 150°C (b).

The growth of Co shell around the FePt core results in higher Msat values at larger particle sizes (r). The size dependence of Msat follows a volumetric power scaling law (r^3) (Figure 3.10a), which is consistent with the increasing volume of Co in the sample and the higher magnetic saturation per unit mass for Co relative to FePt.

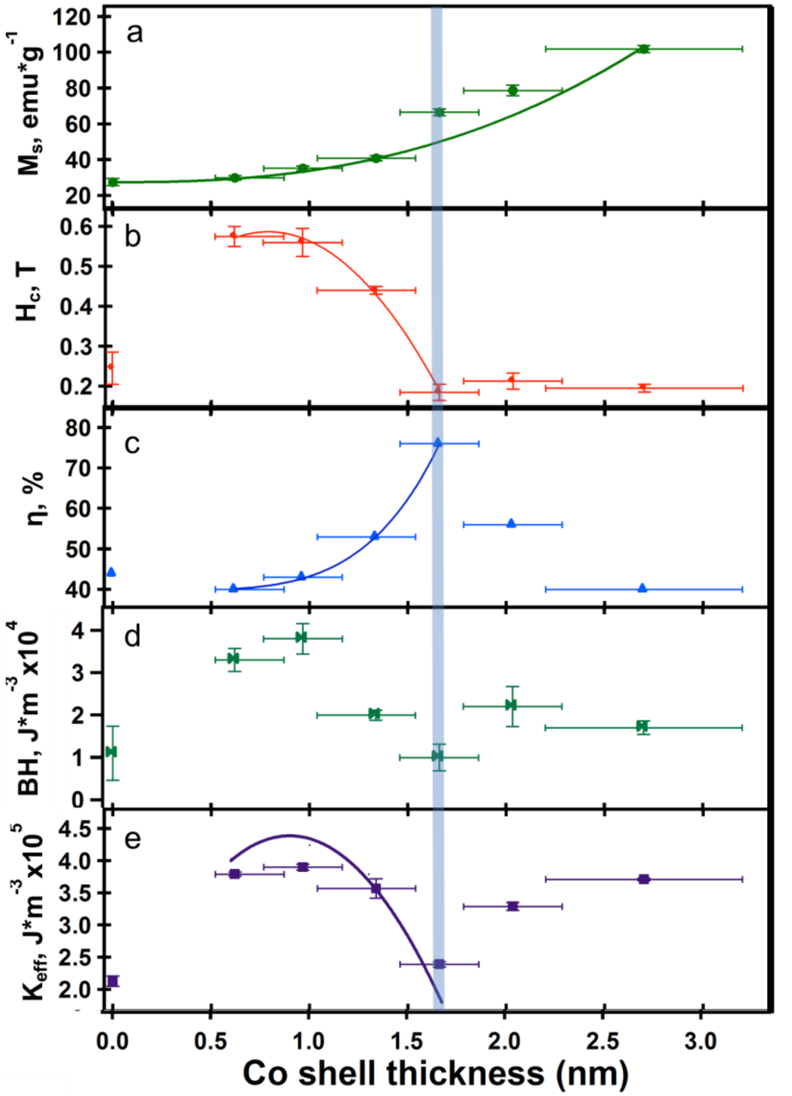

Figure 3.9 The dependence of magnetic properties of FePt@Co nanoparticles on Co shell thickness: (a) saturation magnetization, M_s, (b) coercive field, H_c, (c) % remnant magnetization recovery, (e) energy product, BH, and (e) anisotropy constant, K_{eff}.

In contrast to M_{sat}, the H_c value shows the initial increase at r_{Co} = 0.6 nm followed by a hyperbolic decrease for thicker Co shells (Figure 3.10b). The H_c tends to an asymptote around 0.2 T for shells thicker than 1.7 nm. These changes in H_c can be justified by distance-dependent evolution of exchange behavior between the magnetically hard FePt core and the magnetically soft Co shell. For the thinnest, 0.6 nm Co shell, we observe hard-coupled exchange regime, where the magnetic moments of the shell are pinned by the magnetization of the FePt core. Thus, the Co shell effectively serves to extend the magnetic system of the FePt core, increasing the values of T_B, M_{sat}, and H_c. As the Co shell thickness increases above 0.6 nm, the M_{sat} value continues to grow while the H_c value declines. This effect can be understood by considering the outer Co layers to experience weaker pinning by the FePt core. Therefore, the Co shell thicknesses from 1.0 nm to 1.7 nm might represent the exchange-spring regime. Similar trends in H_c have been observed in nanostructured $HfCo_7$/FeCo[46] and $SmCo_5$/Fe[56] composites.

To probe the existence of the exchange-spring behavior, as defined by Goto, Kneller and Hawig, and Skomski and Coey, the magnetization recovery (η) was measured as a function of shell thickness (Figures 3.9c and 3.10). The η value for the particles with $r_{Co} = 0.6$ nm was identical to that observed for the pure FePt particles (η ~ 40%). For the thicker Co shells, however, η was observed to increase, reaching a maximum value of 75% for $r_{Co} = 1.7$ nm. This finding confirms that the particles composed of the 5-nm fcc-FePt core shelled with the 1.0-nm to 1.7-nm ε-Co shell behave as exchange-spring nanomagnets. (An ideal exchange-spring magnet should have 100% recovery of M_r when the field is turned off.)

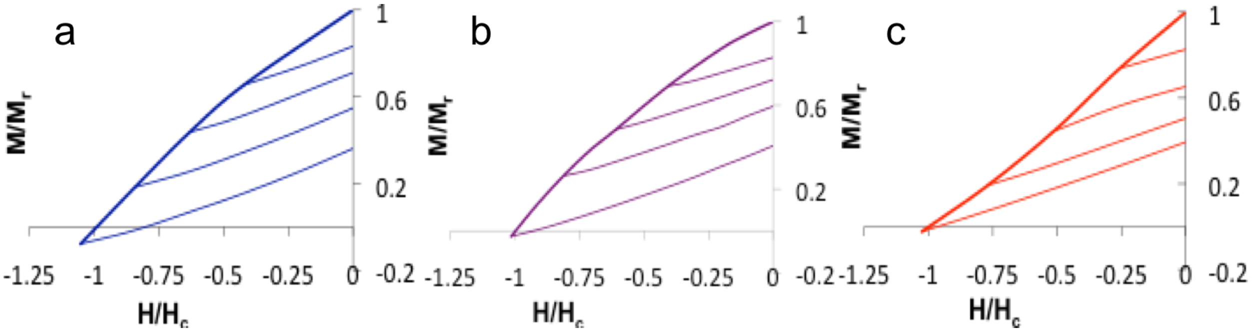

Figure 3.10 Magnetization recovery sweeps of the FePt nanoparticles (a) and the FePt@Co core-shell nanoparticles with 1.0 nm (b) and 2.7 nm (c) Co shell.

We note that our findings compare well to the results of demagnetization sweeps performed on CoPt/Co magnetic bilayers, which demonstrated $\eta \sim 30\text{-}75\%$ after the demagnetizing field was turned off.[70] The maximum in the η value is consistent with the predicted exchange-spring behavior and can be interpreted as occurring at approximately the domain wall width, the distance at which Co moments are still significantly coupled to the hard FePt moments. Beyond this limit, the theoretical model predicts loss of exchange spring behavior, as observed in the experimental data: the η value drops abruptly for $r_{Co} > 1.7$ nm (Figure 3.9c).

An important ramification of the exchange-spring behavior is the expected increase in the energy product. The predicted enhancement of BH in exchange-spring systems has been observed previously in thin-film bilayers and core@shell nanocrystals.[36,49–51] In the present work, the controlled layering of the Co shell onto the FePt core allowed observation of the BH evolution (Figure 3.9d). The BH value increased from 1.10(8) MGOe for the unshelled FePt particles to 3.82(5) MGOe for the FePt@Co particles with 1.0 nm thick Co shell, and then decreased for the particles with thicker Co shell. Thus, the BH is maximized at the point where the H_c remains sufficiently high while the M_{sat} continues to grow. As the shell thickness exceeds 1.0 nm, the continued increase in M_{sat} cannot compensate for the drop in H_c, and the BH value decreases. The growth of the Co shell causes the magnetic moments in its outer layers to become less dependent on the magnetization of FePt core. Therefore, for particles with thicker shells the magnetic behavior becomes dominated by the properties of the shell.

Interestingly, we observed that the evolution of η correlates with the magnetic anisotropy of the system. The latter was calculated as $K_{eff} \approx 2\varepsilon_0 H_c M_{sat}$, where both H_c and M_{sat} are expressed in A m^{-1} and ε_0 is the magnetic permittivity constant, 1.26×10^{-5} T m A^{-1}.[71] The K_{eff}

values as a function of r_{Co} (Figure 3.9e) show a nearly inverse trend as compared to the change in Hc (Figure 3.9c). The calculated K_{eff} of 2.1×105 J m^{-3} for the 4.9 nm FePt cores is comparable to previously reported values for FePt nanoparticles, but it is an order of magnitude lower than the Keff value for the bulk fcc-FePt (2.1×106 J m^{-3}).[72,73] As the Co shell becomes thicker, the K_{eff} decreases towards the value for the bulk ε-Co, 1.5x105 J m^{-3}, until the shell size is above 1.7 nm; above this thickness, the presence of fcc-Co in the outer shell causes the Keff value to approach that of bulk fcc-Co, ~4.2×10^{5} J m^{-3}.[74] The correlation between the minimum K_{eff} and the maximum % recovery at 1.7 nm is a result of stabilizing the H_c while the M_s continues to increase.

3.2.4 Particle Stability

Although no presence of oxide phases could be detected in pXRD patterns of as-prepared nanoparticles, it is well known that a thin layer of oxide can be formed on the surface. In particular, the presence of antiferromagnetic CoO or Co_3O_4 results in exchange-bias effects that manifest themselves in asymmetric hysteresis loops.[75] To probe possible effects of surface oxidation on the magnetic behavior of the nanoparticles, additional magnetic measurements were performed on the unshelled 5-nm FePt cores and the FePt@Co nanoparticles with the 1-nm Co shell, after the particles had been aged for 3 years under ambient conditions and atmosphere (Figure 3.11).

The unshelled FePt cores show no exchange-bias effects even after the 3-year storage, although there is a clear impact on the M_s and M_r values, which changed from 13.5 to 9.5 emu/g and from 7.2 to 4.5 emu/g, respectively. The blocking temperature of the FePt cores decreased from 35 K to 27 K, which is indicative of 4-nm FePt nanoparticles, according to the literature data.[67] Thus, the size of the FePt core effectively decreases due to the surface oxidation (Figure 3.12).

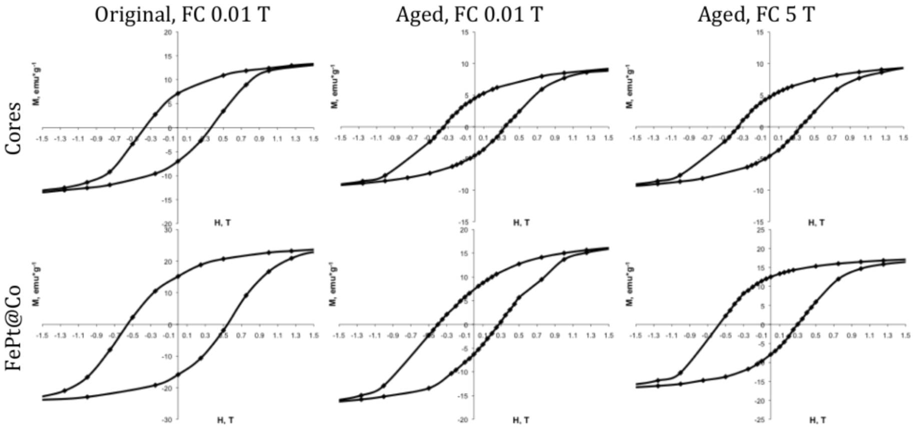

Figure 3.11 Field-dependent magnetization of FePt nanoparticles and FePt@Co nanoparticles with 1 nm Co shell immediately after the synthesis and after 3-year storage in open air.

The FePt@Co sample aged for 3 years showed a clear exchange-bias effect even when being cooled in a 0.01 T applied magnetic field (Figure 3.11). This behavior is attributed to the formation of antiferromagnetic CoO and/or Co_3O_4 on the surface of the particles. The oxide layer, however, is sufficiently thin not to be detected by powder X-ray diffraction. The oxidation of the Co shell caused the decrease in Mr from 15 to 7 emu/g. When the sample was cooled in a 5 T field the exchange bias became even more prominent, with the demagnetization and remagnetization curves crossing the magnetization axis at 0.58 T and 0.3 T, respectively.

The original FePt@Co sample, which was prepared and worked-up under air-free conditions to minimize any oxidation effects, showed only a moderate shift of 0.05 T in the hysteresis loop after being cooled down in a 5 T applied field (Figure 3.13). This observation suggests that the oxidation of the shell during the synthesis and subsequent work-up is minimal, perhaps corresponding to a monolayer of oxide at most forming on the surface of the FePt@Co core-shell nanoparticle. Importantly, the lack of the exchange-bias effect in the as-prepared FePt cores suggests that the in-situ growth of the Co shell guarantees a clean formation of the FePt/Co interface that is not impacted by oxidation. Therefore, the exchange regimes discussed above are governed by the exchange coupling across this interface.

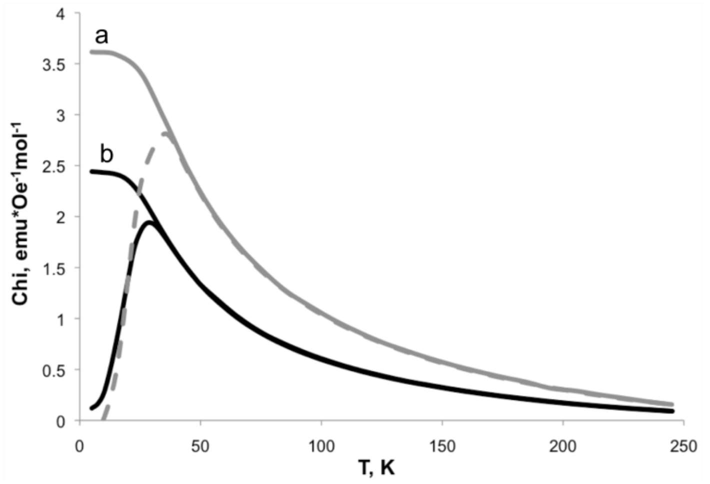

Figure 3.12 Temperature dependences of ZFC/FC magnetization of the original (a) and 3 year old FePt sample (b).

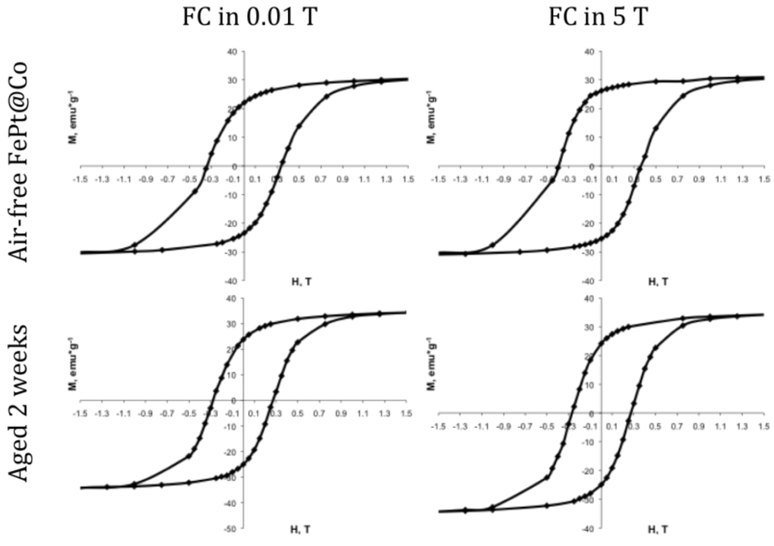

Figure 3.13 Field-dependent magnetization of a FePt@Co sample initially worked up under N_2 atmosphere and then measured again after being held in ambient conditions for 2 weeks.

3.3 Conclusion

In summary, by application of MW-assisted SILAR method, a soft magnet Co shell was layered onto a hard magnet FePt core in a controlled manner, to achieve various shell thicknesses. This process allowed, for the first time, the observation of a correlated enhancement of the coercivity and energy product and other size-dependent exchange regimes in a hard-soft nanocomposite system. Based on the magnetic response of these FePt@Co nanocomposites, the evolution of exchange regimes can be described (Figure 3.14a). Although the actual dimensions will be system dependent, the general behavior is believed to be universal in magnetic hard core@soft shell nanoparticles. The change in the magnetic hardness of the composite (H_c) can be interpreted within the spin-exchange model if the magnetic subsystem is defined over the entire particle.

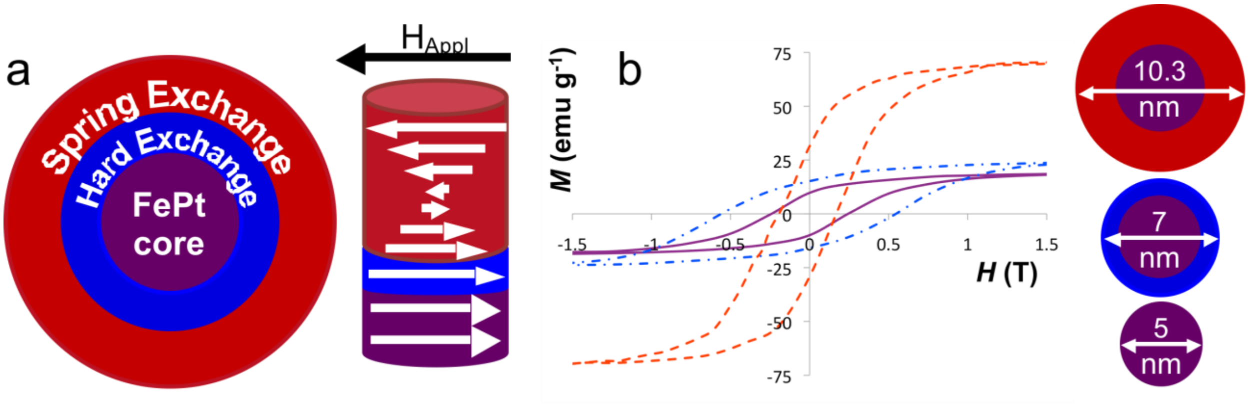

Figure 3.14 (a) A diagram of proposed magnetic exchange regimes that occur within the core-shell nanoparticles. (b) Hysteresis loops for FePt@Co nanoparticles with different Co shell thicknesses.

The assumption of the magnetic behavior being defined by the total system is consistent with the r^3 dependence of M_{sat} and the observation of the single T_B value for the ≥1nm Co-shelled particles. Earlier theoretical models predict a gradual transition from hard-coupled, to exchange-spring, and finally to beyond exchange-spring behavior as one moves away from the magnetically hard core into the magnetically soft shell. The initial increase in H_c is therefore believed to reflect the hard exchange coupling of the 0.6 nm Co soft shell by the $Fe_{0.65}Pt_{0.35}$ hard core resulting in an increased magnetic anisotropy of the total system and a higher coercivity than that of pure fcc-$Fe_{0.65}Pt_{0.35}$ particles.[66,67]

To the best of our knowledge, the evolution between these three regimes has not been reported previously in the nanoparticle literature, which likely is due to the very short range of such behavior. At very short distances ($\leq$ 1.0 nm) from the $Fe_{0.65}Pt_{0.35}$@Co interface, the exchange-pinned Co shell effectively behaves as an extension of the hard FePt core, resulting in the higher H_c values, just like one would observe for FePt nanoparticles of a larger size.[71] As the shell thickness increases, the exchange behavior and magnetic response proceed towards a weaker exchange regime, which first leads to the exchange-spring behavior, and finally to the situation where the outer-most moments of the shell are no longer pinned by the core. Previous work on hard-soft nanocomposites supports the notion that this “unpinning” of the outer moments in larger shells ultimately causes massive losses in the coercivity and generates particles that look more like the soft magnetic materials. Further studies are underway to interrogate the shape and composition effects on the magnetic exchange regimes in these colloidally grown hard-soft magnetic nanocomposites.

CHAPTER 4

EVOLUTION OF EXCHANGE COUPLING BEHAVIOR IN CORE@SHELL MATERIALS WITH VARIABLE CORE SIZES

4.1 Introduction

Initial works in exchange coupling behavior theorizes that the limit of exchange is dictated by the soft magnetic material.[14,55] In order to study this idea multiple FePt core sizes were prepared and were shelled with similar layer of Co in order to see if the particles had similar thickness limits in exchange capabilities. The study involved looking at 3, 5, and 7 nm particles, as they cover a range that transitions from below, at, and above the single domain limit, respectively. These three core sizes will allow us to determine if the stability of the domains within the core particle will have any impact on the stability of the exchange capabilities and limits.

Through use of the microwave shelling procedure previously developed we were able to study the various systems in a well-controlled manner, allowing for a comprehensive study of the different core systems with comparable shell thicknesses. An important determination is if the exchange pathways are truly distance dependent only (shell thickness) or if there are other factors that play a role, like atomic % of the core vs shell.

While exchange-coupled magnetic nanoparticles have been of interest for several decades, little work has been done to study how well the theory holds up, with previous works focusing predominately on what materials can be made, resulting in materials that are outside the limits of enhancement.[31,60,76] It is only recently that experimental studies have put emphasis on the need to keep these systems with thin shells.[29,46] Due to the short exchange distances of soft magnetic nanoparticles, it is found that some unique effects can be found when a thin (<1.5 nm), soft-magnetic shell is applied to a hard-magnetic core.

Extensive work has been performed on fcc-FePt nanoparticles, giving a solid basis for its use as a core material. Through simple modification of reaction conditions, different size and shaped particles can be obtained, allowing for a thorough study of exchange-spring properties utilizing modified cores.[67,77–79] These reactions can be adapted to a microwave procedure in order to allow for rapid screening of different core@shell conditions. Through use of the microwave shelling procedure previously developed we were able to study the various systems in a well-controlled manner, allowing us to study the different systems with comparable shell thickness. An important determination is if the exchange pathways are truly distance dependent only (shell thickness) or if there are other factors that play a role, like atomic % of the core vs shell.

4.2 Results and Discussion

4.2.1 Synthesis

FePt particles of 3.4±0.35, 4.9±0.55 and 7.3±0.65 nm were generated and shelled using modified versions of our previously published microwave synthesis.[80] The 3.4 and 4.9 nm particles were made by using an oleylamine:oleic acid ratio of 6:1 and 4:1, respectively. Similarly, 2.4±0.5 nm particles could be generated when only oleylamine is used as the solvent, however these particles proved difficult to shell, so they're exchange behavior was not fully studied. Larger particles were made by lowering the total concentration of the precursors, where the 7 nm cores formed with a $Pt(acac)_2$ concentration of 0.066M instead of the 0.10M concentration used for the 3.4 and 4.9 nm particles; the $Fe_3(CO)_{12}$ concentration was also lowered to 0.044M (0.133M Fe) to maintain a 2:1 Fe:Pt ratio.

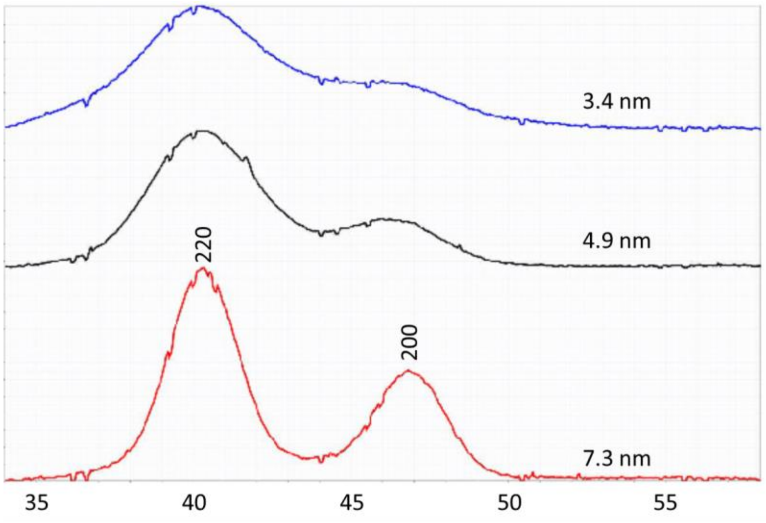

Figure 4.1 Powder XRD patterns of the 3.4 (top), 4.9 (middle), and 7.3 nm (bottom) FePt nanoparticles.

Even larger particles could be made by dropping the concentration to 0.5M Pt(acac)$_2$, however these particles ended up generating octapod shaped particles seen in other FePt syntheses (Figure 4.2d).[78,79]

All of the cores were made using by injecting an amount of their respective stock solution in a microwave vial that was sealed under an N_2 atmosphere; 2mL of stock solution was used for the 3.4 and 4.9nm particles, while 3 mL was used for the 7.3nm particles. The vials were then run in a CEM microwave at 150°C for 5 minutes, at which point air was used to cool the vials to <100°C and then quenched in flowing water. The shelling was done by making a fresh vial of the desired core particles and instead of stopping the reaction at 5 minutes, the shelling solution was injected directly into the microwave vial while the system was continually heated. The in-situ addition reduces the chance for any oxidation between the core and shell, or any subsequent shells added to the particles, as oxidation of the particles will lead to the exchange bias effect and prevent accurate determination of the exchange-hardening enhancement.

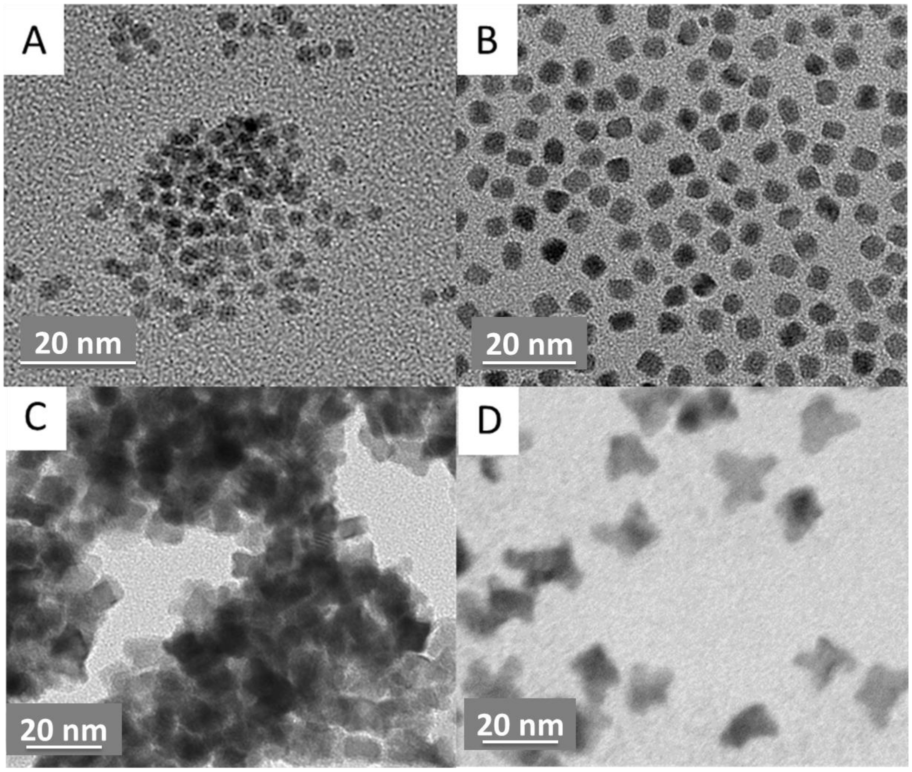

Figure 4.2 TEM of 3.4 nm (a), 4.9 nm (b), 7.3 nm (c), and 10 nm (d) FePt nanoparticles.

While the same total moles of FePt were run in each microwave vial, the differences in surface to volume ratio between the core sizes lead to a significant difference of cobalt being required to shell the different particles. While an addition of 0.2mmol of Co results in 2 layers of Co (~0.6 nm) on the 3 nm particles, the same amount of shelling material used on the 7nm cores resulted in 4 layers (~1.2 nm) of Co added to the surface. Given the ~7mL volume constraint of the microwave vial, this meant that the largest shell sizes of the 3nm particles had to be done by performing an extra clean up and re-dispersion of some of the smaller Co shelled particles and then running them through the microwave an additional time to increase the shell size. On the other hand, the 7nm cores had to be shelled using smaller volumes of Co in order to offset how quickly the shell went on compared to the 5nm cores, which shelled at about 2-3 layers for every 0.2 mmol of Co added.

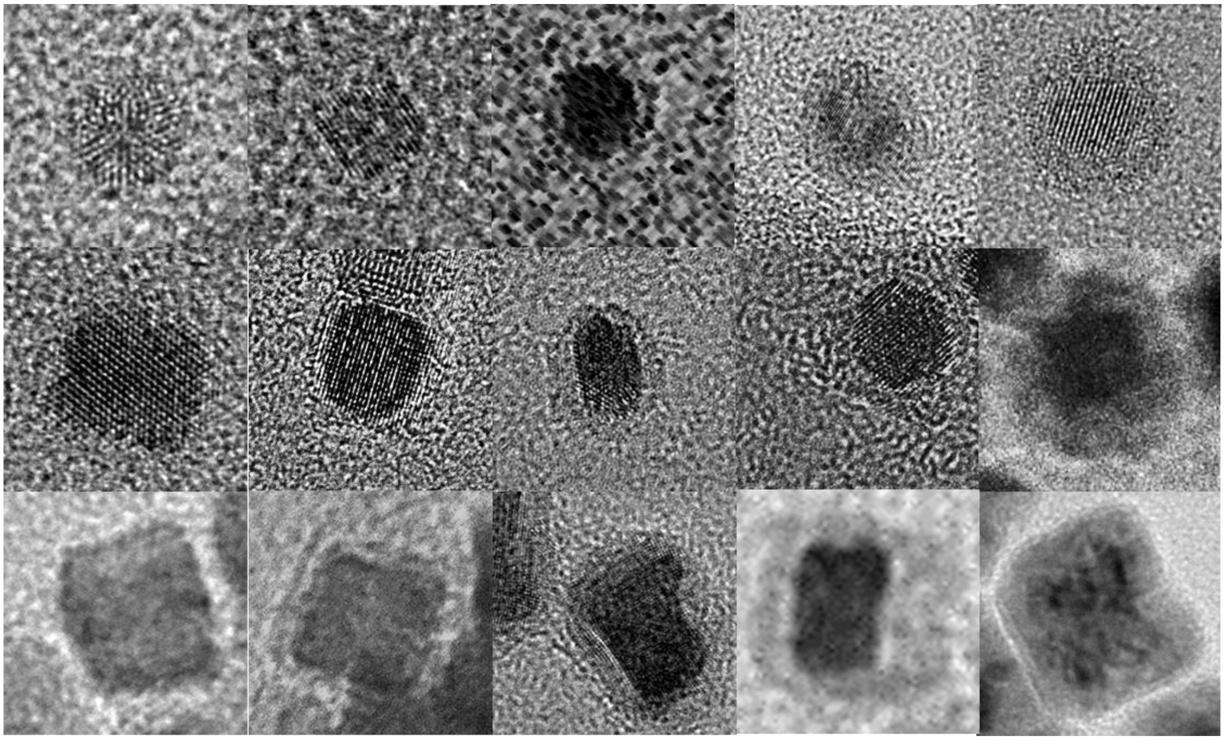

Figure 4.3 TEMs of the various core@shell particles. The top row shows an increasing shell size on the 3.4 nm cores. The middle and bottom rows correspond to the 4.9 and 7.3 nm cores, respectively,

The ability for FePt nanoparticles to form octapods at larger particle sizes lead to issues when synthesizing the 7.3 nm particles.[78,79] If the particles were heated to 150°C too quickly (<1 minute), then the particles tended towards an octopod shape. However, when the reaction was slowed down and allowed to heat to 150°C over the course of 2.5 minutes, the particles formed more in a more cubic shape (Figure 4.2c). Previous work on FePt octapods suggests the shape occurs due to a favorable growth pathway along the [111] edge, similar to what is seen in nickel nanoparticles.[77] In order to improve the shape of the larger particles, the reaction was heated at a slower rate, which lead to more uniform cubic particles that are comparable to the 4.9 nm cores.

4.2.2 Physical Properties

The TGA data shows that the as made 3.4 nm FePt particles are made up of only 9% of ligand by mass. This low ligand content is likely the result of the small surface area of the particles, leading to the oleylamine wrapping around the particle and preventing more from adhering to the surface. Once the particles are reacted in the microwave in the Oleylamine/Oleic solvent mixture, the ligand content of the particles increases drastically to ~17%. Eventually the larger shelled 3.4 nm particles catch up to what's seen in the 4.9 nm particles, reaching upwards of 34% ligand by mass. This is explained by the fact that the low total surface area of the smaller particles causes crowding of the ligands, preventing them from coupling at a high concentration. As the particles get larger and the surface area increases, these particles allow for a higher ligand content on the face of the particles.

The smaller size of the 3.4 nm FePt particles, coupled with the lowered ligand content leads to them being more sensitive to oxidation. Unlike the 4.9 and 7.3 nm particles, the 3.4 nm particles could be seen smoldering due to oxidation when they were completely dried after cleanup. In order to prevent oxidation of the particles before measurements were performed, they were cleaned up in an inert environment and prepared using air-free techniques for SQUID and XRD.

The XRF analysis shows that the particles took on the Fe:Pt ratio that was used to form them in the first place. This results in the core particles all having a 2:1 ratio of Fe:Pt, with only a slight variation in the actual percentages (Table 4.1). The 3.4 nm particles are $Fe_{62}Pt_{38}$, 4.9nm particles are $Fe_{65}Pt_{35}$, and the 7.3 nm particles are $Fe_{63}Pt_{37}$.

Due to the difference in particle size, the ratio of core:shell is not consistent at the same shell sizes. While a 1.5 nm shell on the 3.4 nm core accounts for 88% of the particle by volume, the same 1.5 nm shell size on a 7.3 nm core results in only 66% of the shell by volume. It is along these lines that Hawig and Kneller proposed the limitations of the exchange spring system, where 88% is the best that will be achieved as the shelling material limits the overall range of effect. These changes in ratios account for the observed magnetic properties. While the enhancement to Hc conforms to expectations, with the maximum Hc being seen at ~1 nm of Co shell thickness, the differences in Ms as shell size changes can be attributed to the mass% difference of a 1 nm shell on a 3.4 nm core vs a 7.3 nm core.

Table 4.1 XRF data for comparable shell sizes in each series of particles.

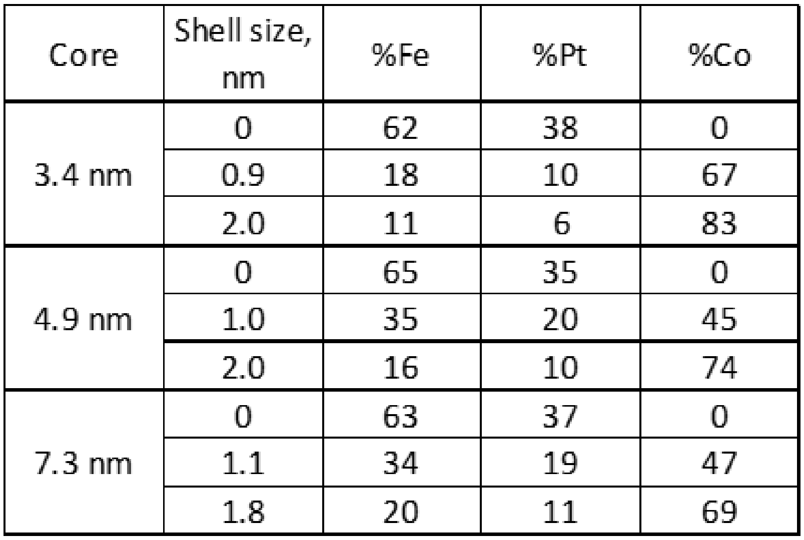

Core	Shell size, nm	%Fe	%Pt	%Co
3.4 nm	0	62	38	0
	0.9	18	10	67
	2.0	11	6	83
4.9 nm	0	65	35	0
	1.0	35	20	45
	2.0	16	10	74
7.3 nm	0	63	37	0
	1.1	34	19	47
	1.8	20	11	69

4.2.3 Magnetic Properties

All three sets of materials show the same capabilities, by transitioning from hard-exchange, to spring-exchange, then finally to decoupled (Figure 4.4). While the actual H_{cmax} and M_{smax} of each system are dependent on the initial FePt core properties, the general behaviors are consistent across all three systems. The saturation magnetization follows a 2.5 to 2.7 power law for all three systems, which is consistent with the expectation that M_s will follow a volume dependent R^3 function (Figure 4.3a). The increase in overall saturation magnetization also follow the expected blocking behavior due to a shift in surface:volume ratio.[70,81,82] The 3.4 nm particles have a 1.76 surface:volume ratio, meaning there are nearly twice as many particles at the surface than there are at the core, making these particles highly susceptible to thermal relaxation. The 4.9 and 7.3 nm particles have a 1.22 and 0.82 ratio, respectively.

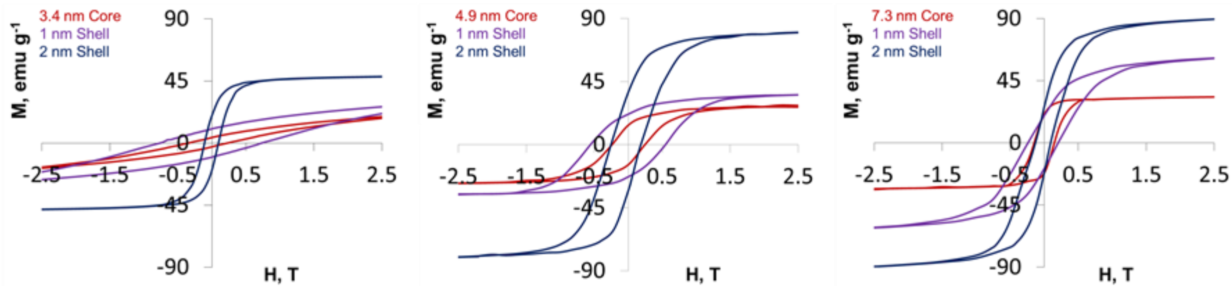

Figure 4.4 Hysteresis loops of the 3.4, 4.9, and 7.3 nm FePt cores, along with their 1 and 2 nm shells.

The variation in surface:volume ratio not only accounts for the increased saturation behavior, but also the increased blocking temperature as particle size increases. The 3.4 nm particles have the lowest blocking temperature at 25 K, with the 4.9 nm cores increasing to 35 K, while the 7.3 nm cores jump up to 85 K. The effect of going from the majority of spins at the surface to the majority of them at the core accounts for large jump in Tb between the 4.9 and 7.3 nm cores, even though there is a comparably small shift between the two smallest sizes.[83,84]

A key feature in all three systems is the ~235% max increase to H_c due to the hard exchange, with the 3nm system increasing from 0.32 to 0.75 T, 5nm from 0.25 to 0.55 T, and 7nm from 0.12 to 0.28 T (Figure 4.6a). Likewise, the maxima occur over a range of 0.8 to 1.0 nm, implying this is the largest distance that cobalt can maintain a strong enough coupling behavior to the core. The lower increase to coercivity for the first shell size in the 3.4 nm cores compared to the other two series is likely a result consistent with the thermal instability of the surface spins. In the same way the core itself is less stable at this size, the exchange behavior is also destabilized at this small particle size.

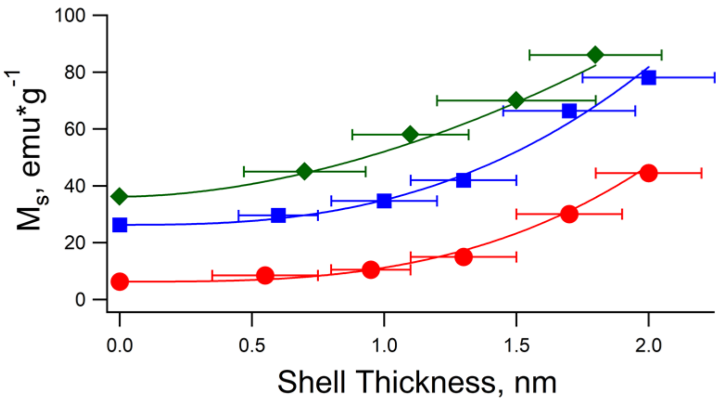

Figure 4.5 The evolution of Ms with increasing shell size. The saturation moment data is fit to a power law consistent with an expected r^3 volume scaling.

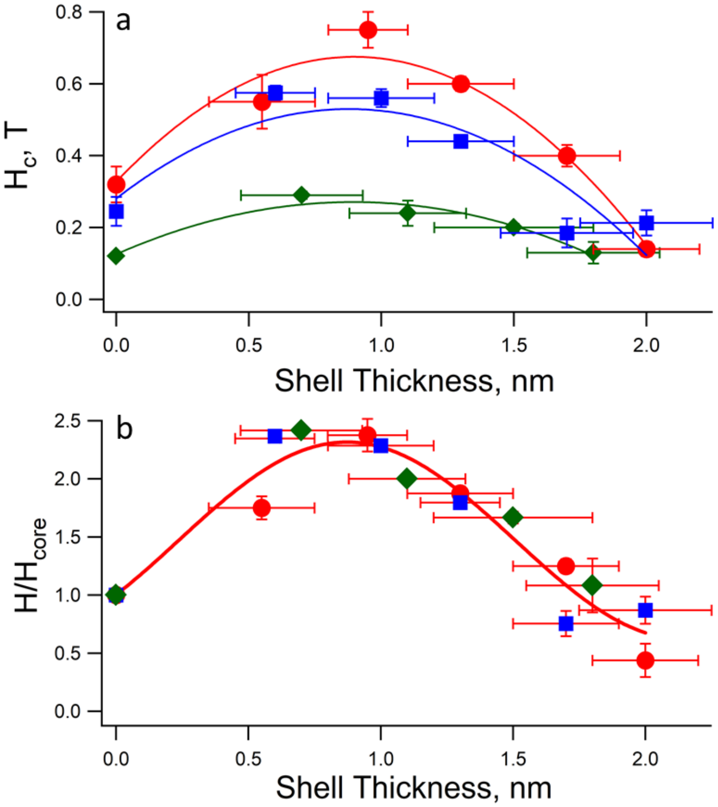

Figure 4.6 The change in H_c with increasing shell size (a) as well as the combined coercivity data after normalizing to the parent core (b). A simple polynomial fit is used as a guide to the eye for (a). The normalized data has been fit to a sine curve in order to determine how well it compares to the idea of a helical spin.

It's in this same vein of thought that it was anticipated that the small size of the 3nm cores would lead to a strongly superparamagnetic behavior, with little coercivity. Instead, the 3.4 nm particles present the highest coercivity of the cores despite the fact that it has super-paramagnetic behavior being seen in the cores, 0.6, and 0.9 nm shelled particles. As the shell sizes get bigger, this behavior levels off due to the shifting surface:volume ratio.

In order to compare the relative effects of shelling on H_c, the coercivity data of each series was normalized based on the parent core particle (Figure 4.6b). From this representation, it can be clearly seen that the effects on coercivity are directly related to the shell of the system, rather than the properties of the core. The one exception that appears is the 3.4 nm@0.6 nm, which doesn't rise as high as initially anticipated. This is likely a result of the size of the particle and the resulting superparamagnetism still seen in the particle even after shelling, resulting in the saturation magnetization of the shell not contributing in the same way that is seen with the larger core systems. By the time the 1 nm shell is put on the particle, making it equivalent in size to the more stable 5 nm system, the expected 236% rise in coercivity is observed.

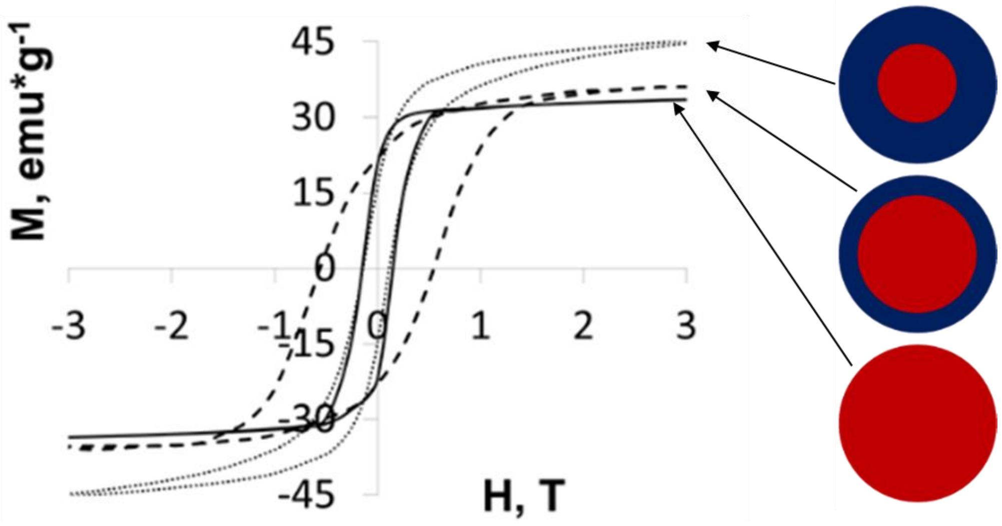

Figure 4.7 Hysteresis loops of the 3.4@2 nm shell, 4.9@1nm shell, and 7.3 nm cores.

The extent that the different exchange properties have on the system can be seen when comparing the different core@shell systems when they're each at 7.3 nm in size (Figure 4.7). This comparison shows how the particle changes between the unshelled 7.3 nm FePt core to the hard exchanged 4.9 nm core@1 nm shell, to the non-exchanged 3.4 nm core@2nm shell. While the 3.4 nm particle shows the highest M_s due to the large Co content, the poor exchange between the core and shell leads to a coercivity that is comparable to a pure 7.3 nm FePt core. The equivalent 4.9 nm core@1nm shell has only a slight increase in Ms compared to the pure 7.3 nm core, but the large increase in coercivity shows the significance of the hard-exchange effect. This comparison shows the necessity of not only shelling material size, but also the core material properties. While the shell will dictate the relative capabilities of the system, it's ultimately limited by the potential of the core system.

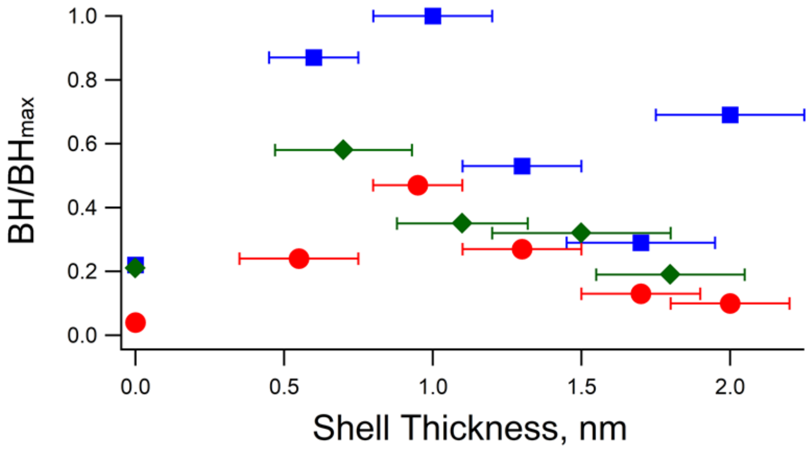

Figure 4.8 The relative energy product of the different particles, normalized to the 5 nm FePt@1 nm Co shell. The 3.4 nm cores are represented in red, the 4.9 nm cores are blue, and the 7.3 nm cores are green.

These results are further confirmed when comparing the energy product of the different particles (Figure 4.8). The original thought process was to find a core with the largest possible coercivity, regardless of saturation magnetization, because the soft magnetic component could offset the limitations of the hard magnetic component. This doesn't work out ideally, as the limitations to exchange length as well as the superparamagnetic effects seen at small sizes, mean that a stable core with average properties is better than a core that is focused on the extremes. Even the 7.3 nm family of particles is able to overcome the 3.4 nm series energy product due to the already higher magnetic magnetization.

4.3 Conclusion

This work shows a clear trend in exchange behavior of the FePt@Co system. Through changing the core size, we were able to alter the initial properties of the shelling system, but still retain the same limitations regardless. A consistent result across all of the core sizes is the doubling enhancement of the coercivity in the hard-exchange regime. The 1 nm shelled particles appear to consistently show the greatest increase in properties, which is consistent with the works of Goto, Hawig and Kneller that suggest the exchange limits are dictated by the soft magnetic component. As the shell thickness increases beyond this point, the particle properties drop off toward the properties of the soft material. However, these results differ from Hawig and Kneller's original proposal that the soft component could exchange over a shell thickness of 2.5 nm (5 nm distance between hard components) and instead show that spring exchange behavior is weaker than the core material by ~1.5 nm. Meanwhile, if the shell is kept at ≤1 nm, then the hard exchange behavior allows for the properties of the core to be enhanced beyond the scope of the hard material by itself.

Another important observation is that although the general enhancement properties are consistent with shell size, the max capabilities of the enhancement are driven by the core properties. In order to have true control over the final magnetic properties of the final system, it becomes essential to expand the selection of hard magnetic materials available for shelling. The introduction of superparamagnetic relaxation is also important, as it prevents the exchange behavior from acting ideally when the particle size gets too small, providing further limitations to what’s allowed for the system.

CHAPTER 5

STUDYING ALTERNATIVE SHELLING ELEMENTS ON A 5 NM FEPT NANOPARTICLE

5.1 Introduction

In order to further study the impact of anisotropy on the interaction between the core and shelling materials, an alternative element was used to shell onto the FePt nanoparticles. The choice to use nickel allows for a oxidation resistant metal that can be applied in the same process that was used to shell with cobalt.[80] Nickel is not often studied in exchange behavior due to its weaker magnetic properties. Instead it is often mixed with some amount of iron and used as a permalloy material in order to increase its magnetic saturation.[85–87] Sun et.al. shelled fct-FePt with nickel previously, however they only studied particles with 6 and 8 nm shell thicknesses, which is well outside any expected hard-exchange limit.[60]

Nickel and cobalt have significantly different anisotropies, -5 kJ/m^3 and 150 kJ/m^3, respectively.[88,89] This difference in magnetocrystalline anisotropy means that the materials have different preferred axes for the magnetic moment to align with. When compared to the positive anisotropy of fcc-FePt, 206 kJ/m^3, the different shells can be expected to generate different interactions with this same core material, depending on the mechanism of the interaction.[74] Work done on FePt/FeNi films have shown a significant difference in the demagnetization process compared to systems with the same sign of anisotropy.[85] Literature work using Fe_3O_4 may give some insight into these issues. Despite its abundant use as a shelling material, Fe_3O_4 has never shown any hard-exchange behavior in FePt@FeOx systems, which may be attributed to its mismatched anisotropy.[27,51,90]

5.2 Results and Discussion

5.2.1 Synthesis

The nickel shell was applied in the same manner that the cobalt shell was applied, where injections from a stock solution could be made into the microwave vial once the core FePt particles had formed. It was found that the smallest shell size that could be put on the particles was a 0.9nm shell. This is believed to have resulted from the magnetic separation used to collect the particles during cleanup. Based on the amount nickel on the particles, compared to how much was used, it means that there were a significant number of unshelled particles that would not be as strongly pulled at room temperature as the Ni shelled particles would. It's possible that this selectivity in shelling is a result from a self-catalytic reaction, where the initial particles that shell with Ni will strongly favor continued shelling compared to the non-shelled particles.

5.2.2 Physical Properties

Since both the core and shell exist as face-centered cubic phases, confirmed by d-spacing measurements, it was expected for the two phases to grow as a cube within a cube. While this does technically happen, TEM shows an unexpected growth pattern in the particles, where the cores appear to grow along a diagonal axis of the fcc-Ni (Figure 5.2). The difference in lattice parameters between the two materials causes the cores to sit as a diamond within a cube style of structure (Figure X). In order to accommodate the 0.32Å difference in lattice parameters between the two fcc structures, the interface goes on at a slant from the core, similar to core@shell quantum dots.[91,92] This structure type will have several implications on the magnetic properties of the material, predominately the fact that this results in the shell size having upwards of 50% variance in thickness depending on if the size is measured from a side or a corner. This variance leads to the shell being seen in the XRD pattern at "shorter" thicknesses.

5.2.3 Magnetic Properties

The temperature sweeps of the different shell thickness are consistent with what was observed with the cobalt studies. As thicker shells of nickel were applied to the particles, an increase in blocking temperature was observed. Given the lower ordering temperature of nickel (355 ˚C) compared to cobalt (1100 ˚C), the increase occurred at a slower pace, resulting in blocking temperatures below room temp even at shell sizes larger than 2nm. The broad range observed in the blocking behavior is one of the effects attributed to the variance in shell thickness that results from the canted alignment between the core and shell (Figure 5.1).

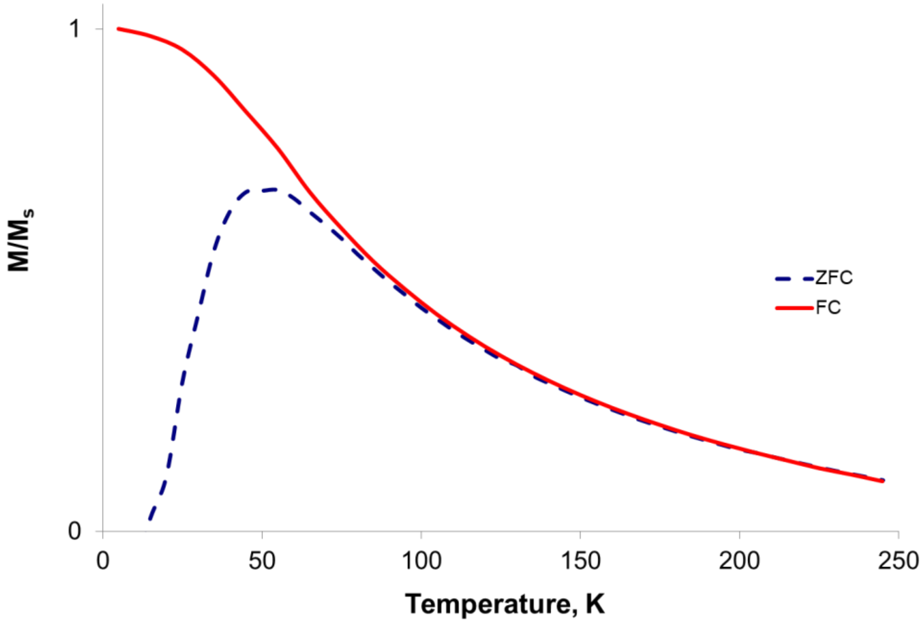

Figure 5.1 ZFC and FC of the 0.9 nm shelled FePt@Ni particles.

The most prominent consequence of the nickel shells can be seen in the field sweeps of the particles. Unlike the cobalt series, the nickel shelling has an impeding effect on the magnetic properties of the FePt. While cobalt shows in increase in both Ms and Hc, the nickel causes a sharp decrease in both properties, drastically decreasing its strength (Figure 5.3). By looking at the changes in saturation magnetization first, some insight into what is happening can be realized. There is an initial drop in M_s of thinly shelled particles, compared to the pure core, despite the fact that nickel has a higher saturation than FePt. The is believed to result from the misaligned structures combined with a difference in anisotropy between the two materials. FePt has a positive anisotropy (K= 206kJ/mol), which means it's magnetic easy axis lies along the <200> axis, however fcc-nickel's negative anisotropy (K= -5.5kJ/mol) meaning the magnetic easy axis lies along the <111> axis.[8,74,88]

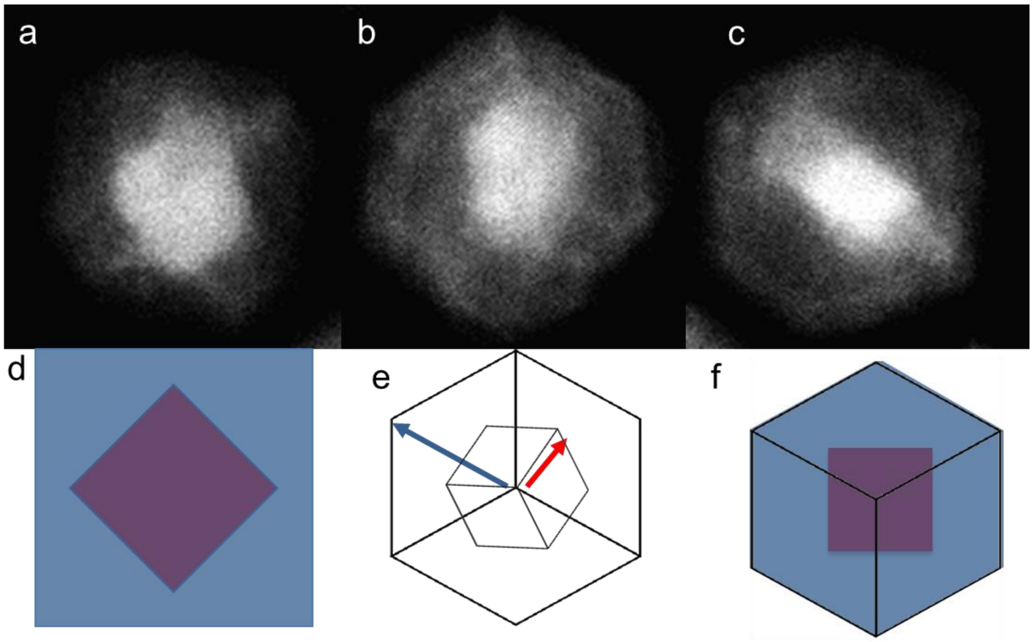

Figure 5.2 STEM images of the 1.5 nm shell (a), and two different angles of the 2 nm shells (b&c), as well as pictorials of the core to shell orientations (d-f), where (e) has a general depiction of the difference in direction between the Ni moments (blue) and FePt moments (red) based on their respective anisotropies.

With these two factors at play, the moments between the core and shell end up being perpendicular to one another, generating a total M_s that is weaker than the individual vectors. Even with the drop in initial magnetization, the M_s still follows an R^3 dependence, suggesting the loss in total magnetization is a constant loss in all of the particles, which is consistent with the idea that the core is subtracting from the total saturation.

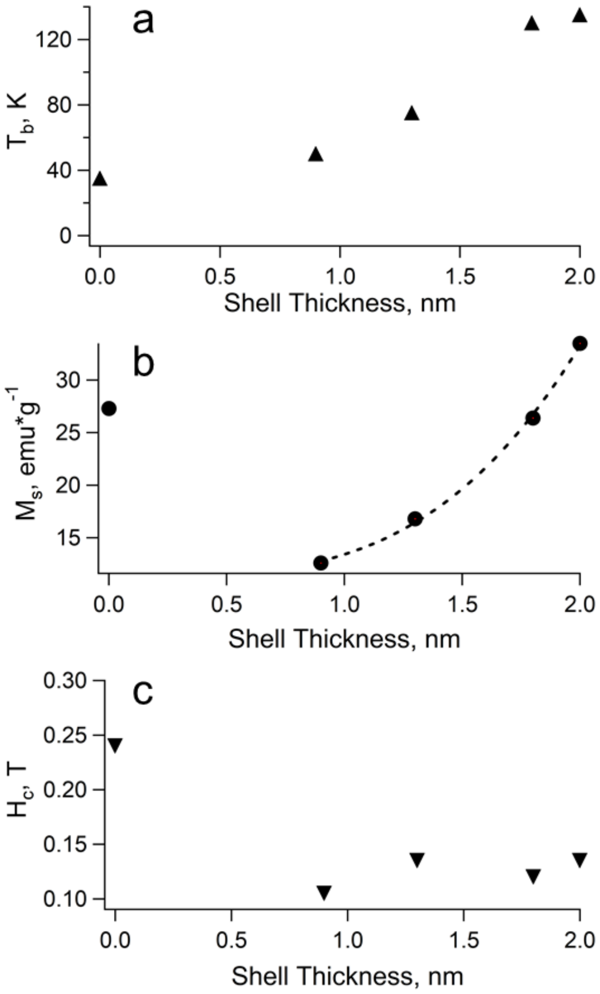

Figure 5.3 Summary of blocking temperature (a), saturation moment (b), and coercivity (c) due to increasing shell thickness of the nickel. The fit of the saturation moment follows an r^3 power law.

This is believed to happen due to a difference in anisotropy between the FePt and the nickel, causing the moments to try and align perpendicular to one another (Figure 5.2e). Looking at the magnetocrystalline anisotropy of FePt, Ni, and Co gives insight into the relation between how coupling is affected by the anisotropy of the core and shell. Both FePt and Co have a positive anisotropy, meaning both have a magnetic easy axis that lies along the <200> axis. However, nickel has a negative anisotropy, which means the easy axis lies along the <111> axis instead. This difference, coupled with the misalignment of the core/shell structures causes the magnetic moments of the two species to be canted in regards to one another (Figure 5.2e).

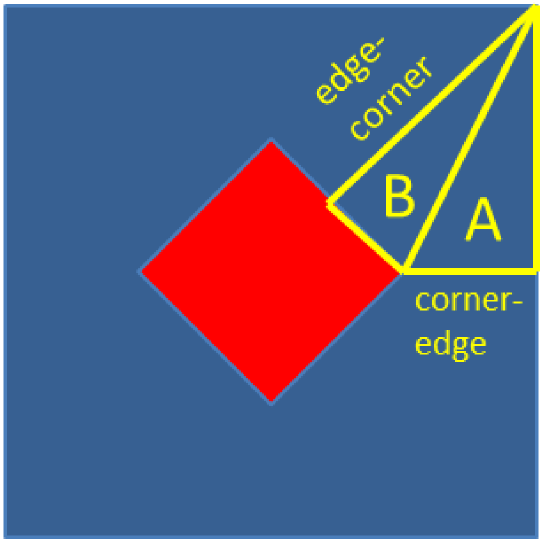

Figure 5.4 Corner-edge and edge-corner distances can be calculated using Pythagorean theorem. The corner-edge distance can be found given the total particle size is known and the core size is known, however the edge-corner distance can only be solved after c for triangle A is found.

Work by Sun et al. showed similar results with their particles, where the 4nm shelled Ni showed a similar Ms to the cores alone and didn't show an increased Ms till a much larger 8nm shell is applied.[60] These results, coupled with the results found with our work, suggests that it requires a significant amount nickel to overcome the dampening effect that occurs from the moment canting.

This diagonal alignment of the cores, in reference to the shell, end up reducing the total coercivity of the system significantly. Given the geometry of the particles in relation of the core to the shell, the Pythagorean theorem can be employed to estimate the corner-edge and edge-corner distances (Figure 5.4). From these calculations, it's found that even with the smallest shell applied, the largest distance is already upwards of 2.3 nm, which is well outside any limits of exchange hardening behavior (Table 5.1). Even though the average shell size is within some anticipated exchange distance, the farthest distance will dominate the relaxation pathway and produce the effects seen in the coercivity. These calculations also provide insight into why the thinnest shelled particles seen are so small and supports what's seen in figure 5.2a, where the shell is almost non-existent at the thinnest, but upwards of ~2nm at the largest sizes. So long as the core and shell remain canted to each other, the shell will either go on with a large diagonal thickness, or cannot fully shell the particle.

Table 5.1 Estimated shortest and longest thicknesses of the FePt@Ni system based on the total particle size.

Avg particle size, nm	Shortest distance, nm	Longest distance, nm	Avg shell thickness, nm
5.0	0.00	0.00	0.00
6.8	0.00	2.31	1.15
7.6	0.27	2.87	1.57
8.6	0.77	3.58	2.17
9.1	1.02	3.93	2.47

An important point to acknowledge is the possibility for the constant drop in coercivity to also be attributed to the canted moments of the particles. Because both moments wish to relax by rotating around some Bloch wall axis, having moments at some angle to one another will provide leverage for the initiation of this relaxation spin. This effect is similar to how exchange bias provides a favorable direction for the core moments to rotate.[93,94] The difference here is that the Ni and FePt moments will always prefer a different angle to one another, while both preferring to be aligned with the field. This will result in a constant relaxation pathway for both magnetization directions, while exchange bias will generate a preferred and a non-preferred direction. Unfortunately, while it's likely that the canted moment may provide some impact to the relaxation pathway of the coercivity, it will require generating particles that are more properly aligned with one another to properly study this effect.

5.3 Conclusion

The series of FePt@Ni shows the impact of poorly matching phases in the core@shell system. These results show the additional limitations to exchange behavior when selecting the core and shell materials, as the combination of a mismatched crystal lattice and magnetocrystalline anisotropy between the two components leads to a canted moment for the total particle. This results in an effect that’s counter to expected results seen with the cobalt system, causing a loss in both saturation and coercivity of the system.[80] The saturation magnetization recovers as more nickel is applied through a constant increase of only one of the magnetic vectors, but at no point does this change the effect on the coercivity. Given that the moments will always be at an angle to one another at all shell sizes, the coercivity will continually be limited.

While this observation appears to add another hurdle for core@shell magnetic exchange to overcome, it also adds the potential of tunability to different systems by controlling the anisotropy of either the core or shell. Using a permalloy-like shell can not only increase the magnetic saturation of the shell, but also shift the saturation magnetization higher than pure fcc-nickel.[85] This may also provide a pathway for epitaxial growth of the shell onto the core, thereby reducing the structural impacts to the magnetic properties.

CHAPTER 6

SYNTHESIS OF OTHER HARD MAGNETIC NANOPARTICLES

6.1 Introduction

A major goal of the project was the generation of high temperature magnetic nanoparticles that could be used in place of the FePt cores. While there is focus on many materials, including $SrFe_{12}O_{19}$, MnBi, and $SmCo_5$, these materials prove to either require high temperature annealing, in the case of $SrFe_{12}O_{19}$, or are simply too unstable in order to shell, as is the case with MnBi. $SmCo_5$ has been a long sought after, but despite numerous attempts over the years many procedures require a post annealing step or rely on ballmilling, which generate particles with poor/no solubility.[58,95,96]

Despite the known issues, we chose to pursue $SmCo_5$ in addition to Fe_3Se_4. Fe_3Se_4 has only recently been a material of interest, with only a couple of labs doing the majority of the work in the past few years.[15,97–101] Most of the work done so far has resulted in particles that are larger than 100 nm and often show little uniformity or contain contaminates in the form of other FeSe phases.[102]

A benefit to both of these materials is that they have more than one composition that results in hard magnetic properties, Sm_2Co_{17} and Fe_7Se_8, improving the chances of successfully generating a usable product.[7,102,103] While these alternative phases exhibit lower coercivity than they're originally targeted counterparts, Sm_2Co_{17} offers an increased saturation magnetization, allowing for tunability in the properties of the shelled particles, should the material be attainable. Likewise, Fe_7Se_8 forms in the hexagonal phase, instead of the monoclinic structure that is obtained with Fe_3Se_4, which may provide a more ideal shelling environment.

6.2 Results and Discussion

6.2.1 Synthesis

Pressure was found to play a critical role in the synthesis of 10 nm SmCo5 particles through standard solvothermal means. When the $Sm(NO_3)_3$ and $CoCl_2$ were reacted without enough pressure present in the reaction, then simple Co particles were synthesized instead. The combination of high pressure and high temperature meant that there were no reliable options in order to run the reaction repeatedly. Both glass and quartz pressure vessels were attempted to no avail. The thick walls of the glass vessel blocked too much of the microwave radiation which prevented it from reaching a high enough temperature. The quartz vessel was able to reach temperature, but the cap was unable to withstand the heat and failed the second time using it.

The Fe_3Se_4 synthesis is believed to form by passing through the intermediate cluster of $[Fe(CO)_3SePh]_2$ (Figure 6.1). This is based on the known reaction between the precursors $Fe_3(CO)_{12}$ and Ph_2Se_2 and the observed differences between how the final material forms when the reaction is rapidly heated to temp instead of allowed to react at an initial lower temp and then heated to the higher reaction temperature.[104] The precursors are first reacted in the microwave at ~100°C for 5 minutes to allow them to interact with one another, followed by heating them at 280°C for another 5 minutes, producing 22 nm Fe_3Se_4 particles. In order to help prove this theory, the Ph_2Se_2 was run by itself in oleylamine, which was a bright yellow solution. Even after 10 minutes at 280°C, there was no noticeable change in the precursor solution, still yielding a bright yellow solution, rather than the dark black solution that would occur were the material react to make selenium nanoparticles. This lack of reactivity supports the idea that the $Fe_3(CO)_{12}$ must first cleave the Se-Se bond, in order to generate a reactive Se species.

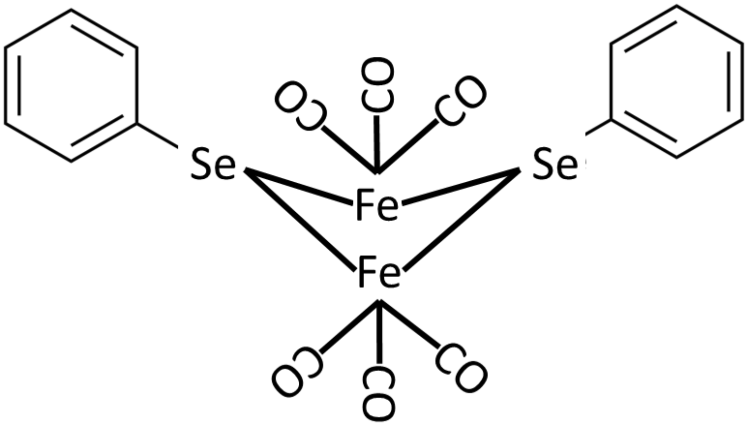

Figure 6.1 Structure of endo-$[Fe(CO)_3SePh]_2$.

On top of the issues that were found with the $SmCo_5$ reaction, both materials have a serious flaw in the microwave due potential plating of the inner walls of the microwave tube. When the reactivity of the transition metals is not controlled well in both syntheses, the cobalt and iron can start plating the vessel, leading to super-heated spots. If the reaction is not cut off the moment this heating begins, the temperature of the reaction will spike within seconds to high enough temperatures that the glass vial will melt.

6.2.2. Structure Characteristics

XRD confirms that $SmCo_5$ was synthesized, although impurities can be seen in the form of Sm_2O_3 and hcp-Co in the $SmCo_5$ pattern (Figure 6.2). The hcp-Co impurities are not surprising, as $SmCo_5$ is a near identical structure, but with vacancies above and below the sites of the samarium. Despite using an initial 3:4 Fe:Se ratio of precursors, the particles actually formed in the mixed structure type with both Fe_3Se_4 and Fe_7Se_8 present. This mixture of phases is a common complication seen with the Fe_xSe_y series.

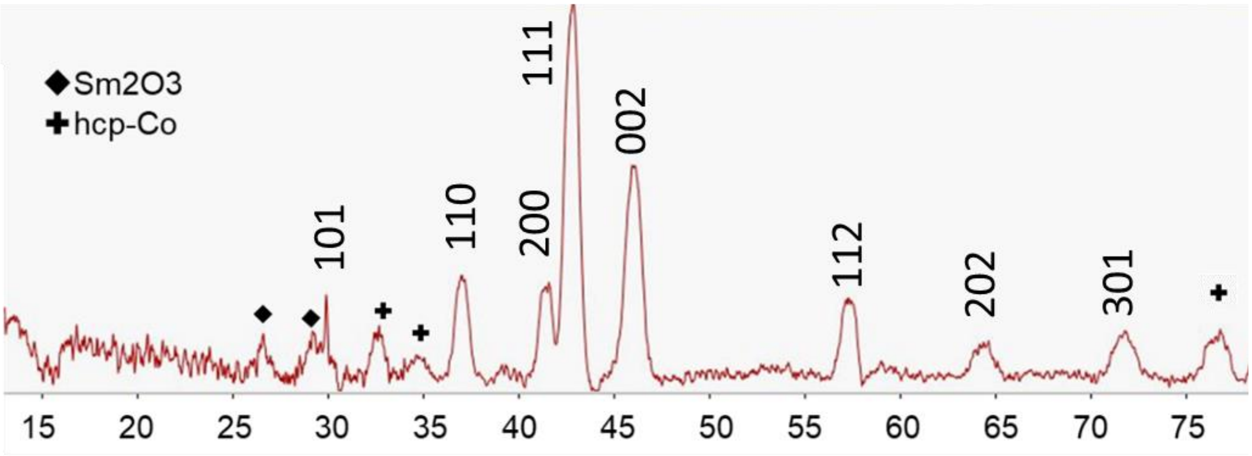

Figure 6.2 XRD pattern for the 10nm $SmCo_5$ nanoparticles. The Sm_2O_3 and hcp-Co impurities are marked, while the hkl planes are given for the $SmCo_5$.[95]

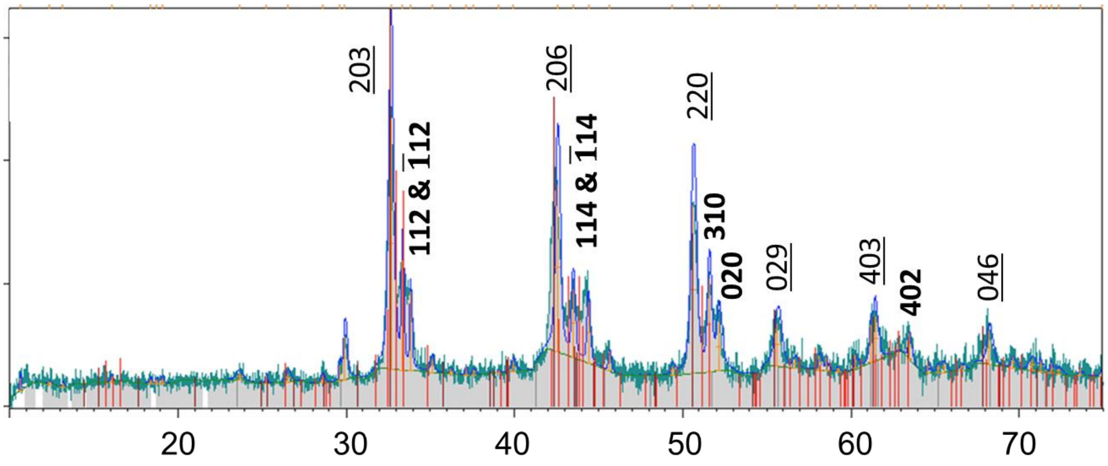

Figure 6.3 XRD pattern of the mixed Fe_3Se_4/Fe_7Se_8 sample. The underlined and bolded hkl labels correspond to the Fe_7Se_8 and Fe_3Se_4 reflections, respectively.[102]

TEM shows the $SmCo_5$ particles formed into bullet shapes that are 10±2 nm. The Fe_3Se_4 particles appear to form round particles that are 22±3 nm. When comparing the particles side by side, there is a clear difference in contrast, implying there's something else going on with the shape of the Fe_3Se_4. Even accounting for the large differences in Z number between the two materials, the large difference in size suggests that the Fe_3Se_4 particles are actually thin plates, rather than spheres. Similar shapes have been seen with Fe_3Se_4, but imaging the particles at an angle would be required in order to confirm this possibility.[15]

The SmCo5 particles are highly soluble in organic solvents, which makes sense given the oleylamine/oleic acid mixture used to synthesize the particles, as well as their relatively low magnetic properties at room temperature. Fe3Se4 on the other hand present with low solubility even though they are synthesized in oleylamine.

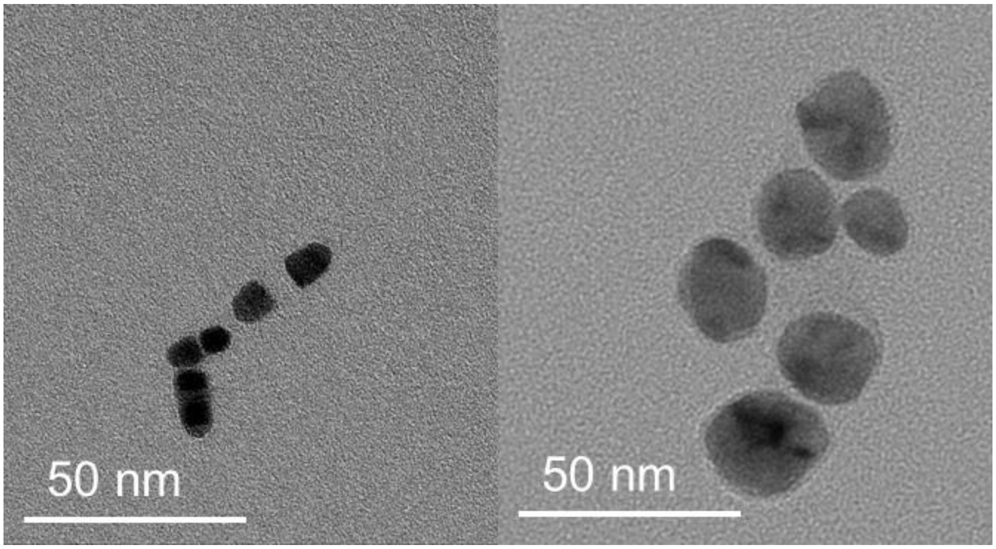

Figure 6.4 TEM of the 10 ± 2 nm $SmCo_5$ particles (left) and the 22 ± 3 nm Fe_3Se_4 particles (right).

6.2.3. Magnetic Properties

Temperature sweeps of the $SmCo_5$ particles reaveal a low blocking temp (Tb) of 6 K, which is well below the 1000 K curie temp of the bulk material.[14] Given the small size of the particles compared to the single domain size of 750 nm for $SmCo_5$, this reuslt seems reasonable.[11,105] These facts also give insight into why the field sweep data shows a low cerocivity of 0.35 T compared to bulk (~80 emu/g, 2.5 T), with a paramagnetic rise to the saturation magnetization.[106]

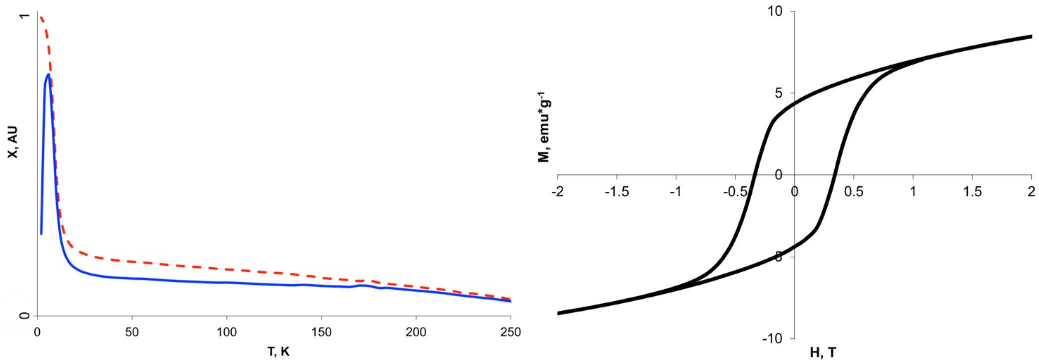

Figure 6.5 ZFC (solid) and FC (dashed) curves for the $SmCo_5$ (left) and the 250 K field sweep (right). The $SmCo_5$ particles show a blocking temp of 6 K and a coercivity of 0.35 T.

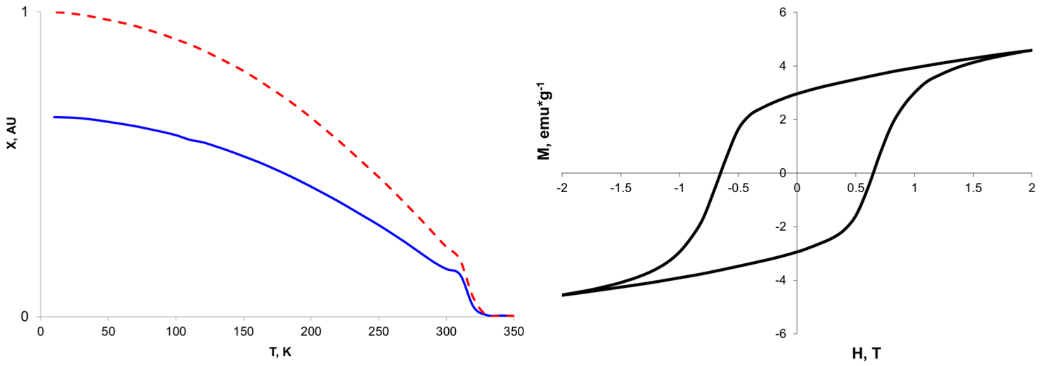

Figure 6.6 ZFC (solid) and FC (dashed) curves for Fe_xSe_y (left) and the 250 K field sweep (right).

The Fe_xSe_y particles show a coercivity of 0.7 T and no appreciable blocking temperature (Figure 6.6). For a mixed phase system, these results are comparable to what would be expected of the bulk material at this temperature. Given the larger size of these particles, these results are reasonable. Were these particles pure Fe_3Se_4, a curie temp closer to 331 K would be expected, with a coercivity upwards of 0.8 T.[100]

6.3 Conclusion

Work with $SmCo_5$ and Fe_3Se_4 in the microwave shows potential for future applications. Uniform $SmCo_5$ particles that are 10nm have been synthesized. The small size and low blocking temperature of these particles (6 K) leads to a 250 K H_c of 0.35 T and M_s of 7 emu/g that is superparamagnetic in nature. The 22nm Fe_xSe_y particles form as a 3:4 and 7:8 mixed phase material. The large particles have a Tc equivalent to bulk (340K) and present with a coercivity of 0.7 T at 250 K.

Serious issues with repeatability need to be addressed for the use of these particles to be practical, including safe and controllable conditions for the $SmCo_5$, as well as reactivity control of the transition metal in both reactions. Should these challenges be overcome, these materials could provide cheaper pathways to generating permanent magnets, specifically $SmCo_5$ which has the potential for high temperature applications.

CHAPTER 7

CONCLUSION AND OUTLOOK

This body of work was written for the purpose of explaining how exchange coupling behavior works between a hard magnetic core and a soft magnetic shell. This was done through systematically varying the core and shell sizes of an fcc-FePt@Co system. To expand upon this work, we used an alternate shelling material as well as synthesized alternate core materials.

In chapter 3, we looked at how varying the shell thickness in a core@shell system affected the exchange properties. As the shell thickness increased, we saw a transition from a system where all of the moments in the shell are coupled to the core (hard exchange), to one with moments that are moderately coupled (exchange-spring), then finally one with little to no coupling behavior (decoupled). The significant findings of this work were, first, that the exchange limits in a core@shell system are much shorter than previously expected and, secondly, that a small enough shell thickness can enhance both the saturation magnetization and the coercivity, compared to the original core. While Hawig and Kneller proposed a system where the exchange-spring behavior works upwards of 2.5 nm, we found that the ideal region for this behavior is closer to 1.7 nm when cobalt is used as the soft magnet. In fact, a 2.5 nm shell will leave the outer moments with very little coupling to the core, producing a particle with coercivity and recovery that is lower than the pure core.

In chapter 4, we find that while the total properties of a hard@soft system are dictated by the properties of the core, the actual exchange limitations are dictated by the soft magnetic shelling material. By incrementally varying either the core or shell size, we found a consistent behavior in the exchange limits. Regardless of core's size, coercivity, or saturation magnetization, the transition between exchange behaviors occurs at the same shell thicknesses. This consistency is clearly shown by the %change to coercivity for each shell thickness, where an initial enhancement of 235% is seen, followed by the same trend in reduction with increasing thickness.

In chapter 5, we found the effects from applying a shell with both an incompatible anisotropy and unit cell. The loss in saturation magnetization is consistent with a core and shell not aligning along the same crystal axes. This reduction is eventually overcome, but only after a significant amount of nickel is applied in order to overcome the constant decrease that the core provides. This canting is likely to play some role in the coercivity as well, but the canted shell growth makes this difficult to confirm. The behavior of the shell growth results in a particle that is outside the anticipated exchange limits, even at the smallest shell applied, thereby preventing a proper analysis of the hard exchange and exchange-spring regimes. In order to fully study how anisotropy of the shell affects exchange behavior, some alternations could be made to the system. In order to prevent the issues with the shell growth, a thin shell of cobalt can be put on first to take advantage of the epsilon phase and then the nickel can be applied after. Given that Co and FePt have similar behaviors in anisotropy, it is reasonable to expect the same kind of losses to M_s, even if the Ni is not directly in contact with the core. Likewise, a Ni_xCo_{1-x} shell can be employed to study how the change in anisotropy of the shell can dictate the magnetic behaviors. The anisotropy of the Ni_xCo_{1-x} system is known to change by varying the ratio of the two metals, allowing us to determine if the transition from a positive to a negative anisotropy is truly necessary to gain the benefits of exchange behavior.[107]

In chapter 6, $SmCo_5$ and Fe_3Se_4 nanoparticle syntheses were explored. While these materials show promise for future applications, the problems with repeatability prevent them from being used for core@shell systems. The issues with repeatability of the $SmCo_5$ reaction could be addressed with some better designed pressure vessels, including a better cap to maintain the pressure as well as employing air to cool the top of the reaction vessel which may help to keep the cap from popping off. The major issue of Fe_3Se_4 is how to ensure the shelling process doesn't cause issues with the crystal structure. This can be improved by picking shelling materials with closer lattice matches to the core, such as Cr_3Te_4, a soft magnetic material with a similar crystal structure to Fe_3Se_4 as well as similar ordering temperature (Table 7.1).[108–110] This choice in material may also prove ideal given the known benefits to the magnetic properties that Cr has on Fe_3Se_4.[100]

Table 7.1. Unit cell parameters and Curie temperature of Fe_3Se_4 and Cr_3Te_4.

	a, Å	b, Å	c, Å	T_c, K
Fe_3Se_4	6.172	3.534	11.195	331
Cr_3Te_4	6.854	3.932	12.255	316

REFERENCES

(1) Lowrie, W. *Fundamentals of Geophysics*, Second.; Cambridge University Press: Cambridge, 2007.

(2) Maxwell, J. C. *A treatise on electricity and magnetism*; 1954; Vol. 53.

(3) Faraday, M. *Philos. Trans. R. Soc. London* **1846**, *136* (0), 1–20.

(4) Bardeen, J.; Cooper, L. N.; Schrieffer, J. R. *Phys. Rev.* **1957**, *108* (5), 1175–1204.

(5) Braunisch, W.; Knauf, N.; Kataev, V.; Neuhausen, S.; Gr̈tz, A.; Kock, A.; Roden, B.; Khomskii, D.; Wohlleben, D. *Phys. Rev. Lett.* **1992**, *68* (12), 1908–1911.

(6) Lee, H. W.; Kim, K. C.; Lee, J. *IEEE Trans. Magn.* **2006**, *42* (7), 1917–1925.

(7) Gutfleisch, O.; Willard, M. A.; Br??ck, E.; Chen, C. H.; Sankar, S. G.; Liu, J. P. *Adv. Mater.* **2011**, *23* (7), 821–842.

(8) Skomski, R.; Coey, J. M. D. *Scr. Mater.* **2016**, *112*, 3–8.

(9) Pan, S. *Rare Earth Permanent-Magnet Alloys' High Temperature Phase Transformation*; Springer Berlin Heidelberg: Berlin, Heidelberg, 2013.

(10) Strnat, K. J. In *New Frontiers in Rare Earth Science and Applications*; Elsevier, 1985; pp 872–878.

(11) Lu, A. H.; Salabas, E. L.; Schüth, F. *Angew. Chemie - Int. Ed.* **2007**, *46* (8), 1222–1244.

(12) Bedanta, S.; Cobalt, C. A. G.; Nanoparticles, F. **1993**.

(13) Klabunde, K. J.; Richards, R. *Nanoscale Materials in Chemistry*; 2001; Vol. 3.

(14) Kneller, E. F.; Hawig, R. *IEEE Trans. Magn.* **1991**, *27* (4), 3588–3600.

(15) Zhang, H.; Long, G.; Li, D.; Sabirianov, R.; Zeng, H. *Chem. Mater.* **2011**, *23* (16), 3769–3774.

(16) Chen, M.; Pica, T.; Jiang, Y. B.; Li, P.; Yano, K.; Liu, J. P.; Datye, A. K.; Fan, H. *J. Am. Chem. Soc.* **2007**, *129* (20), 6348–6349.

(17) Zi, Z. F.; Sun, Y. P.; Zhu, X. B.; Yang, Z. R.; Dai, J. M.; Song, W. H. *J. Magn. Magn. Mater.* **2008**, *320* (21), 2746–2751.

(18) Fullerton, E. E.; Jiang, J. S.; Bader, S. D. *J. Magn. Magn. Mater.* **1999**, *200* (1–3), 392–404.

(19) Bose, S.; Bhattacharyya, A. R.; Kodgire, P. V.; Kulkarni, A. R.; Misra, A. *J. Nanosci. Nanotechnol.* **2008**, *8* (4), 1867–1879.

(20) Gierlings, M.; Prandolini, M. J.; Fritzsche, H.; Gruyters, M.; Riegel, D. *Phys. Rev. B* **2002**, *65* (9), 92407.

(21) Ic, T.; Ic, S. T. *Nature* **2003**, *423* (June), 2–6.

(22) Sun, X.; Huls, N. F.; Sigdel, A.; Sun, S. *Nano Lett.* **2012**, *12* (1), 246–251.

(23) Claudia, A.; Enrico, C. **2010**, *19* (Richter), 576.

(24) Sun, S. *Science (80-.).* **2000**, *287* (5460), 1989–1992.

(25) Elkins, K. E.; Vedantam, T. S.; Liu, J. P.; Zeng, H.; Sun, S.; Ding, Y.; Wang, Z. L. *Nano Lett.* **2003**, *3* (12), 1647–1649.

(26) Wang, H.; Shang, P.; Zhang, J.; Guo, M.; Mu, Y.; Li, Q.; Wang, H. *Chem. Mater.* **2013**, *25* (12), 2450–2454.

(27) Akbari, H.; Sebt, S. A.; Arabi, H.; Zeynali, H.; Elahi, M. *Chem. Phys. Lett.* **2012**, *524*, 78–83.

(28) Delalande, M.; Marcoux, P. R.; Reiss, P.; Samson, Y. *J. Mater. Chem.* **2007**, *17* (16), 1579–1588.

(29) Moon, S. H.; Noh, S. H.; Lee, J. H.; Shin, T. H.; Lim, Y.; Cheon, J. *Nano Lett.* **2017**, *17* (2), 800–804.

(30) Park, J. I.; Kim, M. G.; Jun, Y. W.; Lee, J. S.; Lee, W. R.; Cheon, J. *J. Am. Chem. Soc.* **2004**, *126* (29), 9072–9078.

(31) Zeng, H.; Sun, S.; Li, J.; Wang, Z. L.; Liu, J. P. *Appl. Phys. Lett.* **2004**, *85* (5), 792–794.

(32) García-Cerda, L. A.; Rodríguez-Fernández, O. S.; Reséndiz-Hernández, P. J. *J. Alloys Compd.* **2004**, *369* (1–2), 182–184.

(33) Ma, Z.; Yang, S.; Zhang, T.; Jiang, C. *Chem. Eng. J.* **2016**, *304*, 993–999.

(34) Yu, Y.; Yang, W.; Sun, X.; Zhu, W.; Li, X. Z.; Sellmyer, D. J.; Sun, S. *Nano Lett.* **2014**, *14* (5), 2778–2782.

(35) Kirkeminde, A.; Shen, J.; Gong, M.; Cui, J.; Ren, S. *Chem. Mater.* **2015**, *27* (13), 4677–4681.

(36) Sun, A.-C.; Kuo, P. C.; Hsu, J.-H.; Huang, H. L.; Sun, J.-M. *J. Appl. Phys.* **2005**, *98* (7), 76109.

(37) Huang, J. C. A.; Chang, Y. C.; Yu, C. C.; Yao, Y. D.; Hu, Y. M.; Fu, C. M. *J. Appl. Phys.* **2003**, *93* (10 3), 8173–8175.

(38) Nummy, T. J.; Bennett, S. P.; Cardinal, T.; Heiman, D. *Appl. Phys. Lett.* **2011**, *99* (25), 2014–2017.

(39) Adam, D. *Nature* **2003**, *421*, 571–572.

(40) Galema, S. a. *Chem. Soc. Rev.* **1997**, *26* (3), 233.

(41) Oliver Kappe, C. *Chem. Soc. Rev.* **2008**, *37* (6), 1127.

(42) Washington, A. L.; Strouse, G. F. *J. Am. Chem. Soc.* **2008**, *130* (28), 8916–8922.

(43) Washington, A. L.; Strouse, G. F. *Chem. Mater.* **2009**, *21* (13), 2770–2776.

(44) Ashley, B.; Vakil, P. N.; Lynch, B.; Dyer, C. M.; Tracy, J. B.; Owens, J.; Strouse, G. F. *ACS Nano* **2017**, acsnano.7b04040.

(45) Balamurugan, B.; Das, B.; Zhang, W. Y.; Skomski, R.; Sellmyer, D. J. *J. Phys. Condens. Matter* **2014**, *26* (6), 64204.

(46) Balasubramanian, B.; Mukherjee, P.; Skomski, R.; Manchanda, P.; Das, B.; Sellmyer, D. J. *Sci. Rep.* **2014**, *4*, 6265.

(47) Walmer, M. S.; Chen, C. H.; Walmer, M. H. *IEEE Trans. Magn.* **2000**, *36* (5 I), 3376–3381.

(48) Skomski, R.; Coey, J. M. D. *Phys. Rev. B* **1993**, *48* (21), 15812–15816.

(49) Thiele, J. U.; Maat, S.; Fullerton, E. E. *Appl. Phys. Lett.* **2003**, *82* (17), 2859–2861.

(50) Rheem, Y.; Saito, H.; Ishio, S. *IEEE Trans. Magn.* **2005**, *41* (10), 3793–3795.

(51) Zeng, H.; Li, J.; Liu, J. P.; Wang, Z. L.; Sun, S. *Nature* **2002**, *420* (6914), 395–398.

(52) Son, J. S.; Lee, J. S.; Shevchenko, E. V.; Talapin, D. V. *J. Phys. Chem. Lett.* **2013**, 1–6.

(53) Seemann, K. M.; Bauer, A.; Kindervater, J.; Meyer, M.; Besson, C.; Luysberg, M.; Durkin, P.; Pyckhout-Hintzen, W.; Budisa, N.; Georgii, R.; Schneider, C. M.; Kögerler, P. *Nanoscale* **2013**, *5* (6), 2511.

(54) Lee, H.; Shin, T. H.; Cheon, J.; Weissleder, R. *Chem. Rev.* **2015**, *115* (19), 10690–10724.

(55) Goto, E.; Hayashi, N.; Miyashita, T.; Nakagawa, K. *J. Appl. Phys.* **1965**, *36* (9), 2951–2958.

(56) Hou, Y.; Sun, S.; Rong, C.; Liu, J. P. *Appl. Phys. Lett.* **2007**, *91* (15), 1–3.

(57) Liu, X.; He, S.; Qiu, J. M.; Wang, J. P. *Appl. Phys. Lett.* **2011**, *98* (22), 2011–2014.

(58) Bercoff, P. .; Bertorello, H. . *J. Magn. Magn. Mater.* **1998**, *187* (2), 169–176.

(59) Soares, J. M.; Galdino, V. B.; Conceição, O. L. A.; Morales, M. A.; De Araújo, J. H.; MacHado, F. L. A. *J. Magn. Magn. Mater.* **2013**, *326*, 81–84.

(60) Liu, F.; Zhu, J.; Yang, W.; Dong, Y.; Hou, Y.; Zhang, C.; Yin, H.; Sun, S. *Angew. Chemie - Int. Ed.* **2014**, *53* (8), 2176–2180.

(61) Kim, K. J.; Oleksak, R. P.; Hostetler, E. B.; Peterson, D. A.; Chandran, P.; Schut, D. M.; Paul, B. K.; Herman, G. S.; Chang, C. H. *Cryst. Growth Des.* **2014**, *14* (11), 5349–5355.

(62) Strouse, P. G. F.; Ashley, B. A.; Lovingood, D.; Chiu, Y.-C.; Gao, H.; Owens, J. R. *Phys. Chem. Chem. Phys.* **2015**, *17*, 27317–27327.

(63) Porch, A.; Slocombe, D.; Edwards, P. P. *Phys. Chem. Chem. Phys.* **2013**, *15* (8), 2757.

(64) Peng, Z.; Hwang, J. Y.; Andriese, M. *Appl. Phys. Express* **2012**, *5* (7).

(65) Holzwarth, A.; Lou, J.; Hatton, T. A.; Laibinis, P. E. *Ind. Eng. Chem. Res.* **1998**, *37* (7), 2701–2706.

(66) Sun, S.; Murray, C. B. *J. Appl. Phys.* **1999**, *85* (8), 4325–4330.

(67) Nandwana, V.; Elkins, K. E.; Poudyal, N.; Chaubey, G. S.; Yano, K.; Liu, J. P. *J. Phys. Chem. C* **2007**, *111* (11), 4185–4189.

(68) Thomson, T.; Toney, M. F.; Raoux, S.; Lee, S. L.; Sun, S.; Murray, C. B.; Terris, B. D. *J. Appl. Phys.* **2004**, *96* (2), 1197–1201.

(69) Kim, C. W.; Cha, H. G.; Kim, Y. H.; Abhijit, P.; Jadhav, A. P.; Ji, E. S.; Kang, D. I.; Kang, Y. S. **2009**, 5081–5086.

(70) Murray, C. B.; Sun, S.; Doyle, H.; Betley, T. *MRS Bull.* **2001**, *26* (12), 985–991.

(71) Crew, D. C.; Kim, J.; Lewis, L. H.; Barmak, K. *J. Magn. Magn. Mater.* **2001**, *233* (3), 257–273.

(72) Arcas, J.; Hernando, a.; Barandiarán, J.; Prados, C.; Vázquez, M.; Marín, P.; Neuweiler, a. *Phys. Rev. B* **1998**, *58* (9), 5193–5196.

(73) Seehra, M. S.; Singh, V.; Dutta, P.; Neeleshwar, S.; Chen, Y. Y.; Chen, C. L.; Chou, S. W.; Chen, C. C. *J. Phys. D. Appl. Phys.* **2010**, *43* (14), 145002.

(74) Maenosono, S.; Saita, S. *IEEE Trans. Magn.* **2006**, *42* (6), 1638–1642.

(75) Shukla, N.; Svedberg, E. B.; Ell, J.; Roy, A. J. *Mater. Lett.* **2006**, *60* (16), 1950–1955.

(76) Zeng, H.; Sun, S. *Adv. Funct. Mater.* **2008**, *18* (3), 391–400.

(77) Chou, S. W.; Zhu, C. L.; Neeleshwar, S.; Chen, G. L.; Chen, Y. Y.; Chen, C. C. *Chem. Mater.* **2009**, *21* (20), 4955–4961.

(78) Şimşek, T.; Özcan, S. *J. Magn. Magn. Mater.* **2014**, *351*, 47–51.

(79) Colak, L.; Hadjipanayis, G. C. *Nanotechnology* **2009**, *20* (48), 485602.

(80) Carnevale, D. J.; Shatruk, M.; Strouse, F. **2016**.

(81) Sarkar, T.; Raychaudhuri, a K.; Bera, a K.; Yusuf, S. M. *New J. Phys.* **2010**, *12*, 123026.

(82) Shokuhfar, A.; Afghahi, S. S. S. *Adv. Mater. Sci. Eng.* **2014**, *2014* (1), 10.1155/2014/295390.

(83) Hansen, M. F.; Mørup, S. *J. Magn. Magn. Mater.* **1998**, *184* (3), L262-274.

(84) Singh, S.; Pisane, K. L.; Seehra, M. S. **2017**, 1014–1018.

(85) Davies, J. E.; Hellwig, O.; Fullerton, E. E.; Jiang, J. S.; Bader, S. D.; Zimányi, G. T.; Liu, K. *Appl. Phys. Lett.* **2005**, *86* (26), 1–3.

(86) Lupu, N.; Chiriac, H.; Pascariu, P. *J. Appl. Phys.* **2008**, *103* (7), 2–5.

(87) Hellwig, O.; Hellwig, O.; Kortright, J. B.; Takano, K.; Fullerton, E. E. *Phys. Rev. B - Condens. Matter Mater. Phys.* **2000**, *62* (17), 11694–11698.

(88) Secemski, E.; Anderson, J. C. *J. Phys. D. Appl. Phys.* **1971**, *4* (1), 574–586.

(89) Balela, M. D. L. *Thesis* **2008**.

(90) Margulies, D.; Parker, F.; Spada, F.; Goldman, R.; Li, J.; Sinclair, R.; Berkowitz, a. *Phys. Rev. B* **1996**, *53* (14), 9175–9187.

(91) Zhang, J. *Science* **2012**, *1634* (March), 1634–1639.

(92) Wang, K.; Chen, J.; Zhou, W.; Zhang, Y.; Yan, Y.; Pern, J.; Mascarenhas, A. *Adv. Mater.* **2008**, *20* (17), 3248–3253.

(93) Soares, J. M.; Galdino, V. B.; Machado, F. L. A. *J. Magn. Magn. Mater.* **2014**, *350*, 69–72.

(94) Stiles, M. D.; McMichael, R. D. *Phys. Rev. B* **2001**, *63* (6), 64405.

(95) Hou, B. Y.; Xu, Z.; Peng, S.; Rong, C.; Liu, J. P.; Sun, S. *Adv. Mater.* **2007**, *19* (20), 3349–3352.

(96) Pal, S. K.; Schultz, L.; Gutfleisch, O. *J. Appl. Phys.* **2013**, *113* (1).

(97) Li, D.; Li, S. J.; Zhou, Y. T.; Bai, Y.; Zhu, Y. L.; Ren, W. J.; Long, G.; Zeng, H.; Zhang, Z. D. *J. Appl. Phys.* **2015**, *117* (17), 1–5.

(98) Sen Bishwas, M.; Das, R.; Poddar, P. *J. Phys. Chem. C* **2014**, *118* (8), 4016–4022.

(99) Li, D.; Jiang, J. J.; Liu, W.; Zhang, Z. D. *J. Appl. Phys.* **2011**, *109* (7), 2014–2017.

(100) Li, S.; Li, D.; Liu, W.; Zhang, Z.; Sun, S.; Murray, C. B.; Weller, D.; Folks, L.; Moser, A.; Rong, C. B.; Li, D.; Nandwana, V.; Poudyal, N.; Ding, Y.; Wang, Z. L.; Zeng, H.; Liu, J. P.; Hou, Y.; Xu, Z.; Peng, S.; Rong, C.; Liu, J. P.; Sun, S.; Atsushi, O.; Hirakawa, K.; Hirone, T.; Maeda, S.; Tsuya, N.; Tokutaro, H.; Chiba, S.; Hirakawa, K.; Grønvold, F.; Westrum, E. F.; Andresen, A. F.; Laar, B. V.; Akihiko, H.; Katsuhiro, I.; Kazumichi, I.; Yutaka, U.; Koji, K.; Kojima, K.; Murase, S.; Sato, K.; Adachi, K.; Kojima, K.; Matsui, M.; Sato, K.; Adachi, K.; Snyder, G. J.; Caillat, T.; Fleurial, J. P.; Li, D.; Jiang, J. J.; Liu, W.; Zhang, Z. D.; Long, G.; Zhang, H. W.; Li, D.; Sabirianov, R.; Zhang, Z. D.; Zeng, H.; Zhang, H. W.; Long, G.; Li, D.; Sabirianov, R.; Zeng, H.; Wang, J.; Duan, H.; Lin, X.; Aguilar, V.; Mosqueda, A.; Zhao, G.; Bishwas, M. S.; Das, R.; Poddar, P.; Holland, T. J. B.; Redferna, S. A. T.; Delgado, G. E.; Sagredo, V.; Kang, J. H.; Kim, S. J.; Lee, B. W.; Kim, C. S.; Lamarche, G.; Bulyzhenkov, I.; Wang, P.; Quintero, M.; Lamarche, A. M.; Takemura, Y.; Suto, H.; Honda, N.; Kakuno, K.; Saito, K.; Brouha, M.; Buschow, K. H. J.; Miedema, A. R.; Coey, J. M.; Sun, H. J.; Takahashi, H.; Igawa, K.; Arii, K.; Kamihara, Y.; Hirano, M.; Hosono, H.; Yang, J. L.; Ren, W. J.; Li, D.; Hu, W. J.; Li, B.; Zhang, Z. D.; Zhang, G. Q.; Zhang, T.; Lu, X. L.; Wang, W.; Qu, J. L.; Li, X. G. *Nanoscale* **2015**, *7* (12), 5395–5402.

(101) Andresen, A. F.; van Laar, B.; Kvamme, E.; Ohlson, R.; Shimizu, A. *Acta Chemica Scandinavica*. 1970, pp 2435–2439.

(102) Lyubutin, I. S.; Lin, C.-R.; Funtov, K. O.; Dmitrieva, T. V.; Starchikov, S. S.; Siao, Y.-J.; Chen, M.-L. *J. Chem. Phys.* **2014**, *141* (4), 44704.

(103) Boumford, C.; Morrish, A. H. *Phys. Status Solidi* **1974**, *22* (2), 435–444.

(104) Shermer, E. D.; Baddley, W. H. *J. Organomet. Chem.* **1971**, *30* (1), 67–73.

(105) Hadjipanayis, G. C. *J. Magn. Magn. Mater.* **1999**, *200* (1–3), 373–391.

(106) Rong, C.; Poudyal, N.; Liu, X. B.; Zhang, Y.; Kramer, M. J.; Ping Liu, J. *Appl. Phys. Lett.* **2012**, *101* (15), 2010–2013.

(107) Fan, W.-J.; Ma, L.; Shi, Z.; Zhou, S.-M. *Chinese Phys. B* **2015**, *24* (3), 37507.

(108) Ohta, S.; Kaneko, T.; Yoshida, H. **1996**, *3*.

(109) Andresen, A. F. *Acta Chemica Scandinavica*. 1968, pp 827–835.

(110) Yamaguchi, M.; Hashimoto, T. *J. Phys. Soc. Japan* **1972**, *32* (3), 635–638.

BIOGRAPHICAL SKETCH

a. Professional Preparation

Graduate: Florida State University Inorganic / Materials Chemistry. **Ph.D., 2017**

Thesis Title: Synthesis and Characterization of Magnetic Exchange-Spring Composites
Advisor(s): Professor Michael Shatruk, Professor Geoffrey F. Strouse

Undergraduate: Clark University **B. A., 2009**

Organometallic Coordination Chemistry
Advisor: Professor Mark Turnbull

b. Work Experience

Florida State University	Graduate Student Assistantship	**2011-present**
Shire Human Genetic Therapies	Cell Biology Technician II	**2009 –2011**
	Stability Technician 1	**2009**
	Quality Control Intern	**2007 –2009**

c. Awards/Achievements

2016 – Nominated for FSU Outstanding TA Award

2014 – Dept. of Chemistry Outstanding General Chemistry TA Award

2012 – Dept. of Chemistry Outstanding General Chemistry Laboratory TA Award

2003 - Eagle Scout

d. Publications (Total papers: 8; 5 first author, 3 co-author)

1) **Carnevale, D.;** Landee, C.; Turnbull, M.; Winn, M.; Xiao, F.; "Co(II) Halide Complexes with 2-amin-3-methylpyridinium and 2-amino-5-methylpyridinium: Synthesis, Crystal Structures, and Magnetic Properties", *Journal of Coordination Chemistry* **2010,** 63, 2223
2) **Carnevale, D.**; Shatruk, M.; Strouse, G. F.; "Ligand Passivated Core-Shell FePt@Co Nanomagnets Exhibiting Enhanced Energy Product", *Chem. Mater.* **2016**, 28, 5480.
3) **Carnevale, D.**; Shatruk, M.; Strouse, G. F.; "Size dependent effects in the Core@Shell Magnetic Exchange Spring Phenomenon" (In preparation)
4) **Carnevale, D.**; Pierce, C.; Hardy, D.; Strouse, G. F.; "Synthesis of Bimetallic Nanoparticles from single source PBA clusters" (In preparation)
5) **Carnevale, D.**; Shatruk, M.; Strouse, G. F.; Doping effects on the structural and magnetic properties of the M_3Se_4 system (In preparation)

e. Oral Presentations

1) **David Carnevale**, Michael Shatruk, and Geoffrey F. Strouse. “Modifying Magnetic Properties in Core@Shell Nanoparticles”. ACS National Meeting and Exposition. August 2016. Philadelphia, PA
2) **David Carnevale**, Michael Shatruk, and Geoffrey F. Strouse. “Probing Magnetic Exchange Regimes in Core@Shell Nanoparticles”. Florida Inorganic Materials Seminar. October 2015. Gainesville, FL
3) **David Carnevale**, Michael Shatruk, and Geoffrey F. Strouse. “Controlling Hard/Soft Magnetic Exchange in Core/Shell Nanoparticles”. ACS National Meeting and Exposition. August 2015. Boston, MA
4) **David Carnevale**, Michael Shatruk, and Geoffrey F. Strouse. “Synthesis of Nanosized Permanent Magnets”. ACS South West Regional Meeting. November 2012. Baton Rouge, LA

f. Poster Presentations

1) **David Carnevale**, Michael Shatruk, and Geoffrey F. Strouse. “Plotting the Limits of Core/Shell Magnetic Exchange”. Joint ACS SERMACS-SWRM Regional Meeting. November 4, 2015. Memphis, TN
2) **David Carnevale**, Michael Shatruk, and Geoffrey F. Strouse. “Synthesizing Nanoscale Permanent Magnets”. Florida Solid State Chemistry meeting. October 2012. Tallahassee, FL
3) **David Carnevale**, Michael Shatruk, and Geoffrey F. Strouse. “Synthesis of Nanoscale Permanent Magnets”. Poster Presentation, American Chemical Society National Meeting and Exposition. August 20, 2012. Philadelphia, PA

g. Expertise

Florida State:

Microwave-based Syntheses, Nanoparticle Synthesis, TEM, DSC, Schlenk Techniques, XRD, SQUID

Shire Human Genetic Therapies:

Operating under Good Manufacturing Practices (GMP), HPLC (SEC, Glycan Mapping), ELISA, Coomassie-PAGE, Western-PAGE, Cellular Uptake, generating SOP’s

Clark University:

Crystallization, Crystallography, IR